Biomaterials 335 (2026) 124368



Contents lists available at ScienceDirect

Biomaterials

journal homepage: www.elsevier.com/locate/biomaterials



Antibiotic-drug conjugates: Enhancing chemo-immunotherapy of gemcitabine for pancreatic cancer by eliminating intratumoral bacteria

Ziyao Zhang [a], Fangming Zhang [a], Wangting Yang [a], Jingxia Xu [a], Zhuyuan Peng [a], Xinyu Zhao [b], Yen Wei [b], Guofeng Li [a,*], Wensheng Xie [a,**], Xing Wang [a,***]

[a] The State Key Laboratory of Organic-Inorganic Composites, The Beijing Laboratory of Biomedical Materials, College of Life Science and Technology, Beijing University of Chemical Technology, Beijing, 100029, PR China

[b] The Key Laboratory of Bioorganic Phosphorus Chemistry & Chemical Biology (Ministry of Education), Department of Chemistry, Tsinghua University, Beijing, 100084, PR China

ARTICLE INFO

Keywords:
Antibiotic-drug conjugate
Pancreatic cancer
Intratumoral bacteria
Gemcitabine
Chemo-immunotherapy

ABSTRACT

Pancreatic cancer has a dismal five-year survival rate of only ~13%, owing to its insidious onset, rapid progression, and frequent primary or acquired resistance to gemcitabine (Gm). Moreover, intratumoral bacteria capable of expressing cytidine deaminase (CDD) can undermine the therapeutic efficacy of Gm and contribute to chemoresistance. To address this challenge, antibiotic-drug conjugates (AiDCs, Tob–SS–Gm NPs) were developed by covalently linking tobramycin (Tob) and Gm via disulfide bonds. Tob–SS–Gm NPs retained antibacterial activity against *E. coli* and chemotherapeutic activity in Panc02 cells, indicating that the conjugation preserves the functional properties of both components. Meanwhile, disulfide linkage enables these AiDCs to remain stable under physiological conditions while undergoing cleavage in the high GSH tumor microenvironment, thereby releasing Tob and Gm for coordinated antibacterial and antitumor effects. *In vivo* evaluation demonstrated that Tob–SS–Gm NPs effectively reduced intratumoral bacterial burden and were associated with improved therapeutic response to Gm under bacteria-colonized tumor conditions. Furthermore, bacterial elimination and tumor cell damage were accompanied by modulation of the tumor immune microenvironment, including enhanced dendritic cell maturation and increased cytotoxic $CD8^+$ T-cell infiltration. Collectively, this AiDCs strategy provides a promising approach for the treatment of intratumoral bacteria-associated, drug-resistant malignancies.

1. Introduction

Pancreatic cancer is one of the most aggressive and lethal malignancies, with a median survival of approximately four months and a five-year survival rate of only 13% [1,2]. Due to its insidious onset, rapid progression, resistance to existing therapies, and poor drug penetration [3,4], significant breakthroughs in pancreatic cancer treatment have remained elusive. Gemcitabine (Gm), the current first-line chemotherapeutic drug, efficiently extends survival in some patients [5]. However, its clinical benefit is greatly limited by the low overall efficacy and by the rapid development of resistance[6–8]. Therefore, developing effective therapeutic strategies to directly overcome Gm resistance has become a major focus for pancreatic cancer treatment.

Multiple studies have revealed that intratumoral microbial colonization is widespread in pancreatic cancer tissue [9,10]. Intestinal-derived Gram-negative bacteria, in particular, can migrate via the bile duct or bloodstream and persist long-term in pancreatic tissues [11]. These intratumor-colonizing bacteria express metabolic enzymes, such as cytidine deaminase (CDD), to deaminate Gm into inactive metabolites, thereby reducing its efficacy efficacy of Gm and also increasing drug resistance [8,12]. Therefore, eliminating the intratumor microbiota is considered a potential strategy to improve chemotherapy sensitivity and prolong patient survival for pancreatic cancer[13–18].

Antibiotics are the gold standard for anti-microbial treatment in clinic. However, excessive use of antibiotics may disrupt the gut microbiota, leading to adverse reactions such as diarrhea, indigestion,

* Corresponding author.
** Corresponding author.
*** Corresponding author.
E-mail addresses: ligf@mail.buct.edu.cn (G. Li), xws@mail.buct.edu.cn (W. Xie), wangxing@mail.buct.edu.cn (X. Wang).

https://doi.org/10.1016/j.biomaterials.2026.124368
Received 1 January 2026; Received in revised form 13 May 2026; Accepted 5 June 2026
Available online 12 June 2026
0142-9612/© 2026 Elsevier Ltd. All rights are reserved, including those for text and data mining, AI training, and similar technologies.

gastrointestinal disorders, and inflammation[19–21]. Moreover, an ideal combination of antimicrobial and chemotherapeutic therapies requires the spatiotemporally coordinated delivery of antibiotics and chemotherapy drugs16,22–24. In recent years, conjugated drugs have garnered widespread attention in precision cancer therapy due to their advantages, such as spatiotemporally controlled delivery of multiple drugs [25–28]. Moreover, the dynamic linkers such as disulfide bonds, ester bonds, or Schiff base bonds enable the site-specific activation of prodrugs in the targeted site[29–35]. Therefore, the development of a conjugated drug that integrates antibacterial and chemotherapeutic performances is of great significance in reducing the burden and improving efficacy of pancreatic cancer, yet remains highly challenging.

Herein, to eliminate the intratumor bacteria during pancreatic cancer chemotherapy, an antibiotic-drug conjugate (AiDCs) strategy was employed to construct self-assembled nanodrugs (Tob–SS–Gm NPs) based on Tob and Gm via a dynamic disulfide bonding (Scheme 1A). After conjugation, Tob–SS–Gm NPs exhibited effective *in vitro* antibacterial activity against *E. coli* and chemotherapeutic activity against Panc02 cells, fulfilling the dual functional requirements of antibacterial-assisted chemotherapy. After internalization by tumor cells, the dynamic disulfide bond enables rapid cleavage of the conjugate in the high GSH tumor microenvironment, thereby releasing Tob and Gm for synchronized antibacterial and antitumoral activity (Scheme 1B). The released Tob effectively reduces intratumoral bacterial burden and improves the therapeutic response to Gm under intratumoral bacteria-colonized conditions. In addition, bacterial eradication and tumor cell damage further reshape the tumor immune microenvironment and are associated with enhanced DCs maturation and cytotoxic $CD8^+$ T-cells activation. In the present study, this immune remodeling is more directly supported by DAMP-associated immunogenic signals, while the contribution of bacterial PAMP-related pathways warrants further investigation.

2. Experimental section

2.1. Experimental materials

3,3′-Dithiodipropionic acid (DDA), glutathione (GSH), and gemcitabine (Gm) were purchased from TCI. Tobramycin (Tob) was purchased from Energy Chemical. Pluronic F-127 (F-127) was purchased from Aladdin. 1,2-Benzenedicarboxaldehyde (OPA) was purchased from Innochem. The Annexin V-FITC/PI Apoptosis Detection Kit, TRITC-Phalloidin, Cell Migration and Invasion Stain Kit (For Transwell) and 4′,6-diamidino-2-phenylindole (DAPI) were purchased from Solarbio (Beijing, China). Lysogeny broth (LB) and lysogeny agar (LA) were purchased from Sigma-Aldrich. Bovine serum albumin (BSA) and Triton X-100 were purchased from Solarbio Science & Technology Co., Ltd. (Beijing, China). SYTO9/propidium iodide (PI) was purchased from Thermo Fisher Scientific. The PE anti-mouse CD11c antibody, FITC anti-mouse CD80 antibody, APC anti-mouse CD86 antibody, PE anti-mouse CD3 antibody, PC5.5 anti-mouse CD4 antibody, and FITC anti-mouse CD8 antibody were purchased from BioLegend (USA).

2.2. Characterizations

The ^{1}H NMR spectra of all polymers were acquired using a Bruker 400 MHz spectrometer in either D_2O or DMSO-d_6 at room temperature. The size and zeta potential of the nanoparticles were evaluated via dynamic light scattering (DLS) using a Malvern Zetasizer Nano ZS 90. Transmission electron microscopy (TEM, HT-7700, Hitachi, Japan) and scanning electron microscopy (SEM, JSM-7800F, JEOL, Japan) were used to examine the morphologies of the nanoparticles and bacteria. UV-vis spectra were obtained using a UV-vis spectrometer (U4100, Hitachi, Japan). Cellular uptake and apoptosis were monitored using a confocal laser scanning microscope (CLSM, Leica SP8, Germany) and a flow cytometer (Beckman Coulter, Ltd). *In vivo* imaging was conducted using a Caliper Life Sciences (USA) Xenogen *In vivo* Imaging System (IVIS).

2.3. Synthesis of Tob–SS–Gm, Tob–SS–Tob and Gm–SS–Gm

Tob (4 mmol) and DMAP (0.4 mmol) were dissolved in DMSO (30 mL). DDA (8 mmol) and EDCL (4 mmol) were separately dissolved in DMSO (5 mL). After activation at 41°C for 25 min, the two solutions were combined and reacted at 41°C for 24 h. The crude product was concentrated and precipitated with excess ice-cold methanol to obtain Tob–SS–OH. Tob–SS–Gm was then synthesized by coupling Tob–SS–OH with Gm using the same esterification procedure. Tob–SS–Tob and Gm–SS–Gm were synthesized analogously.

2.4. Preparation and characterization of NPs

The nanoparticles were prepared using the two-phase interfacial self-assembly method, with Pluronic F-127 as the stabilizer. Briefly, Tob–SS–Gm was dissolved in DMSO. While F-127 was dissolved in deionized water. The aqueous phase was then slowly added to the organic phase under controlled conditions to induce nanoparticle self-assembly. Suspension was transferred into a dialysis bag and dialyzed against deionized water for 24 h to remove the organic solvent and unassembled molecules. The dialyzed product was subsequently lyophilized to obtain Tob–SS–Gm NPs. Tob–SS–Tob NPs, Gm–SS–Gm NPs, C6@Tob–SS–Gm NPs, and Cy7@Tob–SS–Gm NPs were prepared using the same procedure. Since Tob and Gm are linked at a fixed molar ratio of 1:1 in Tob–SS–Gm NPs, the Tob–SS–Gm NPs concentrations were expressed as equivalent drug concentrations.

The hydrodynamic diameter, size distribution, and zeta potential of the nanoparticles were determined by dynamic light scattering (DLS, Zetasizer Nano ZS, Malvern, UK). Morphological characterization was performed by scanning electron microscopy (SEM, JSM-7800F) and transmission electron microscopy (TEM, HT-7700).

2.5. GSH-responsive behavior of NPs

A solution of 3,3-dithiodipropionic acid (10 mM, 5 mL) was prepared, and then DTT (10 mM, 5 mL) was added. Next, Tob–SS–Gm NPs, Tob–SS–Tob NPs, and Gm–SS–Gm NPs (10 mg/mL, 5 mL) were added to the solution. Samples were taken at specific time points to evaluate the performance of their reduction response. 200 μL of the reaction mixture was mixed with OPA (10 mM, 100 μL), and the absorbance was measured at 338 nm. Because direct use of GSH may interfere with OPA-based thiol detection, DTT was used here as a model reducing reagent to evaluate disulfide cleavage *in vitro*.

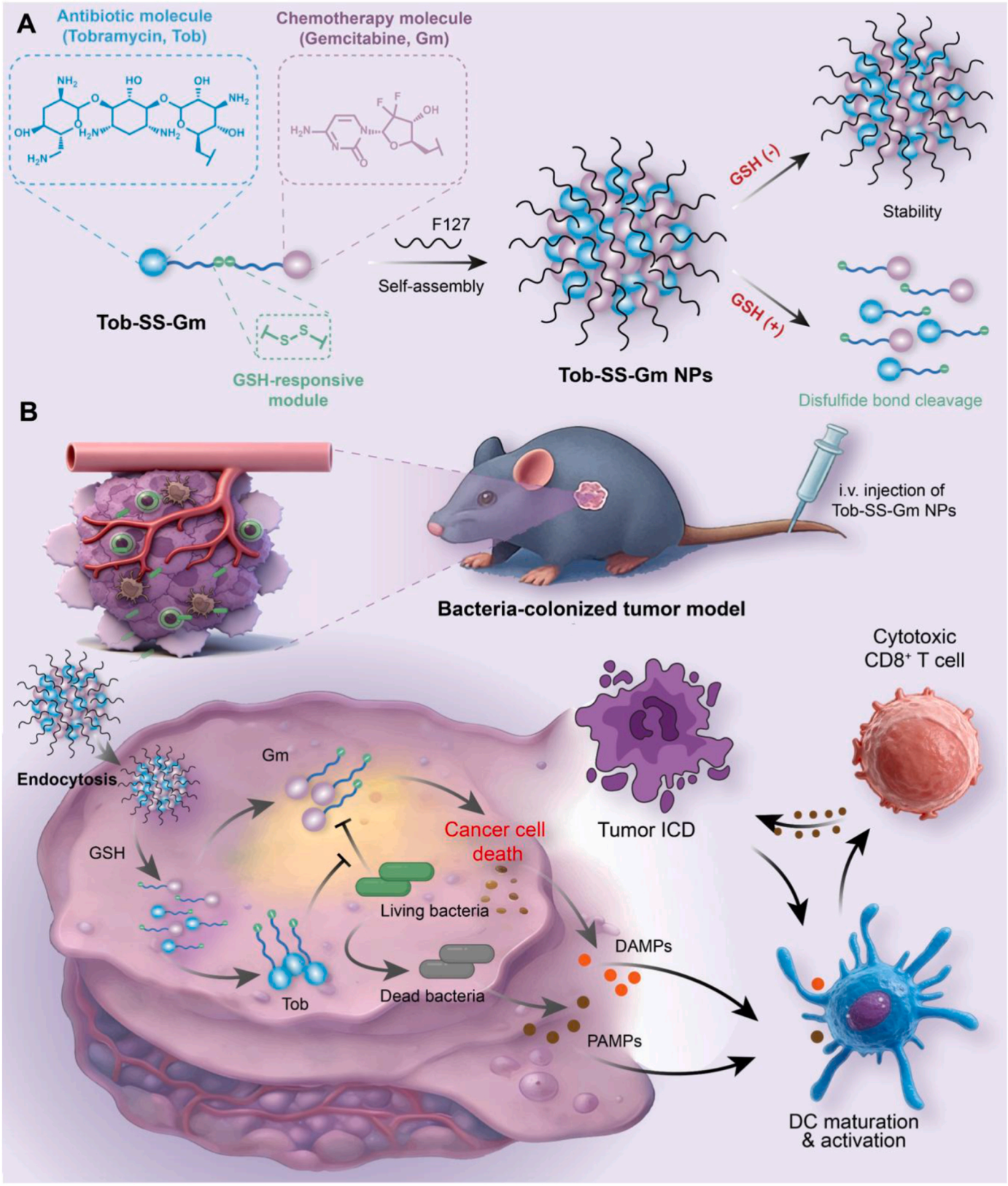
2.6. In vitro MIC determination and MBC determination

E. coli was used as the model bacterium in this study. A single bacterial colony was picked from an agar plate and inoculated into LB medium, followed by incubation at 37°C with shaking at 180 rpm for 8 h to obtain bacteria in the logarithmic growth phase.

Tob, Tob–SS–Gm NPs, and Tob–SS–Tob NPs were separately dissolved in sterile water to prepare the corresponding stock solutions. Twofold serial dilutions were then prepared in MHB using a 96-well plate. Log-phase bacteria were diluted with sterile saline to 1×10^6 CFU/mL, and 100 μL of the bacterial suspension was added to each well containing 100 μL of the drug solution, resulting in a final volume of 200 μL per well. The plate was incubated at 37°C for 24 h, after which bacterial growth was evaluated by measuring the absorbance at 600 nm.

2.7. Co-localization assay of NR@Tob–SS–Gm NPs with E.coli

Bacteria in the logarithmic growth phase were diluted with sterile saline to a concentration of 1×10^8 CFU/mL. Subsequently, 1 mL of



Scheme 1. Schematic illustration of enhancing chemo-immunotherapy of Gm for pancreatic cancer by eliminating intratumoral bacteria via antibiotic-drug conjugates (AiDCs). (A) Construction of Tob–SS–Gm AiDCs via GSH-responsive disulfide bonding and self-assembled nanostructure. (B) Tob–SS–Gm NPs are activated by elevated GSH in the tumor microenvironment to release Tob and Gm simultaneously. Tob helps eliminate intratumoral bacteria and thereby relieve bacteria-associated Gm resistance. Dead bacteria and treatment-damaged cancer cells may further remodel the tumor immune microenvironment, thereby promoting dendritic-cell maturation and cytotoxic $CD8^+$ T-cell activation.

SYTO9 was added, and the mixture was incubated for 2 h. Then, 1 mL of medium containing NR@Tob–SS–Gm NPs was added and incubated for an additional 2 h. After incubation, the mixture was centrifuged and washed, followed by observation and analysis using a microscope slide.

2.8. In vitro antibacterial activity

Multiple methods were employed to investigate antimicrobial activity. Initially, bacteria in the logarithmic growth phase were diluted to a concentration of 1×10^6 CFU/mL using sterile physiological saline. Different treatment drugs were then added to establish the following experimental groups: control, Tob, Tob–SS–Gm NPs, and Tob–SS–Tob NPs. Each bacterial suspension was cultivated in a shaker at 37°C and 180 rpm. Samples were collected at predetermined time points, and the OD_{600} at 600 nm was measured to assess bacterial growth. After 12 h, 100 μL of bacterial suspension from each group was subjected to serial dilutions and spread onto LB solid plates to count CFU.

To further characterize the bacterial responses to the treatments, live/dead staining using SYTO9 and PI was performed, with observations made under confocal microscopy. Additionally, bacterial morphology was examined through SEM.

2.9. Determination of the zone of inhibition

Bacterial suspensions were uniformly spread onto agar plates containing the appropriate culture medium. Sterile filter paper disks were then placed on the agar surface, and a fixed volume of each antibacterial formulation was added onto the corresponding disk. After incubation at 37°C for 24 h, the diameters of the inhibition zones were measured and compared to evaluate the antibacterial activity of the different formulations.

2.10. Anti-bacterial biofilm performance assay

Bacteria in the logarithmic growth phase were diluted to 1×10^6 CFU/mL with sterile physiological saline. Then, 500 μL of the bacterial suspension and 500 μL of TSB containing 1% glucose and 5% NaCl were added to a 48-well plate and incubated at 37°C for 48 h to allow biofilm formation. After incubation, the medium was discarded, and 1 mL of culture medium containing different drugs was added. The plate was further incubated for 24 h. The mixture was then washed, and 1 mg/mL crystal violet solution was added for staining for 2 h. After drying, 30% (v/v) acetic acid was added to elute the biofilm, and the absorbance at 595 nm was measured using a microplate reader. For three-dimensional confocal imaging, biofilms grown in confocal dishes were incubated with SYTO9 and PI dyes at 4°C in the dark for 20 min. After washing to remove unbound dyes, the samples were observed and analyzed using a confocal microscope.

2.11. In vitro anticancer efficacy and biosafety evaluation

The mouse pancreatic cancer cell line Panc02 and the human fibroblast cell line L929 were used in this study. Both cell lines were cultured in RPMI 1640 medium supplemented with 10% FBS and 1% penicillin-streptomycin under standard cell culture conditions.

For the CCK-8 assay, Panc02 and L929 cells in the logarithmic growth phase were seeded into 96-well plates at a density of 8000 cells per well and cultured for 24 h. The cells were then treated with Gm, Tob–SS–Gm NPs, Tob–SS–Tob NPs, or Gm–SS–Gm NPs at various concentrations (96, 48, 24, 12, 6, 3, and 1.5 μg/mL) for an additional 24 h. Subsequently, CCK-8 working solution was added to each well, and the absorbance at 450 nm was measured using a microplate reader to determine cell viability.

2.12. In vitro anticancer efficacy evaluation

To investigate cellular uptake, Panc02 cells were seeded in 35 mm glass-bottom dishes at a density of 1×10^5 cells per well and cultured for 24 h. The cells were then incubated with medium containing either C6@Tob–SS–Gm NPs or free C6 for 1, 4, 8, or 24 h. After incubation, the cells were washed twice with PBS, fixed, permeabilized, and sequentially stained with TRITC-phalloidin and DAPI. Cellular uptake was then observed using confocal laser scanning microscopy.

To evaluate treatment-induced cytotoxicity, Panc02 cells were further subjected to live/dead staining with Calcein-AM and PI, followed by confocal imaging. In parallel, Annexin V-FITC/PI staining was performed according to the manufacturer's instructions, and the stained cells were analyzed to assess apoptosis.

2.13. In vitro cell motility measurement

Panc02 cells in the logarithmic growth phase were harvested and adjusted to a density of 2×10^5 cells. A 100 μL aliquot of the cell suspension was seeded into the upper chamber of each Transwell insert, while 500 μL of complete medium containing 10% FBS and the designated formulation was added to the lower chamber. After 48 h of incubation, the inserts were removed, and the cells remaining on the upper surface of the membrane were gently removed with a PBS-soaked cotton swab. The migrated cells on the lower surface were fixed with methanol for 20 min, stained with 0.1% crystal violet for 30 min, rinsed thoroughly, and air-dried. Images were captured using an inverted microscope, and the number of migrated cells was quantified using ImageJ software.

2.14. Antibacterial activity in vitro against intracellular bacteria

Panc02 cells were seeded into 24-well plates at a density of 1×10^5 cells per well. Log-phase *E. coli* was collected and used to infect the cells at a bacteria-to-cell ratio of 10:1. After 2 h of infection, extracellular bacteria were removed by gentamicin treatment. The cells were then incubated for 24 h with culture medium containing the designated formulations, including Control, Tob, Gm, Tob + Gm, Tob–SS–Gm NPs, Tob–SS–Tob NPs, and Gm–SS–Gm NPs. After treatment, the cells were lysed, and the lysates were serially diluted 1000-fold. A 100 μL aliquot of each diluted sample was spread onto LB agar plates for bacterial colony counting. To further evaluate intracellular bacterial status and tumor-cell responses after treatment, live/dead staining with Calcein-AM and PI was performed and observed by confocal microscopy. In parallel, Annexin V-FITC/PI staining was carried out to assess apoptosis.

2.15. Three-dimensional spheroid culture and drug treatment in SpheroX™ 96U plate

Each well of the SpheroX™ 96U plate was pretreated with 100 μL of anti-adhesion coating solution and incubated overnight. After removal of the coating solution, 100 μL of cell suspension containing 10000 cells per well was seeded into the coated wells and cultured for 1 week to allow spheroid formation. The medium was then replaced with fresh culture medium containing the designated formulations, and incubation was continued for 6 days. On day 6, the spheroids were stained with calcein for 20 min, gently washed with PBS, and observed using confocal microscopy.

2.16. In vivo biosafety evaluation

Female C57BL/6 mice (6–8 weeks old) were purchased from Beijing VITONLIV Co., Ltd. The animals were housed under standard conditions (22 ± 2°C, 50% ± 10% humidity, 12 h light/12 h dark cycle) with free access to food and water. All animal procedures were performed in accordance with the National Research Council's Guidelines for the Care

and Use of Laboratory Animals and were carried out according to the guidelines and protocol (DLASBD0513) approved by the Institutional Animal Care and Use Committee of Peking University Health Science Center.

For biosafety evaluation, female C57BL/6 mice were randomly divided into three groups (n = 5 per group). The treatment groups received Tob–SS–Gm NPs (2 mg/mL or 10 mg/mL) via tail-vein injection, while the control group received an equal volume of PBS. The formulations were administered every 2 days. On day 14, blood samples were collected for serum biochemical analysis. The levels of aspartate transaminase (AST), alanine aminotransferase (ALT), alkaline phosphatase (ALP), serum urea (UREA), and blood urea nitrogen (BUN) were measured to evaluate hepatic and renal function.

2.17. In vivo drug targeting capability and bacterial tumor colonization ability

Female C57BL/6 mice (8 weeks old) were housed for 1 week before use. A subcutaneous Panc02 tumor model was established by injection of 2×10^6 Panc02 cells. Once the tumor volume reached approximately 100 mm^3, the mice were randomly divided into two groups. One group received Cy7@Tob–SS–Gm NPs via tail-vein injection, whereas the other group received free Cy7. *In vivo* fluorescence imaging (IVIS) was performed at 0, 6, 9, 12, and 24 h after administration. At 12 h post-injection, the mice were euthanized, and the heart, liver, spleen, lung, kidney, and tumor tissues were collected for ex vivo fluorescence imaging.

To evaluate bacterial tumor colonization, mice bearing Panc02 tumors of approximately 200 mm^3 received 100 μL of *E. coli* suspension (1×10^6 CFU/mL) via tail-vein injection. The animals were euthanized on days 1, 3, 5, and 7 after bacterial injection. Tumor tissues and major organs, including the heart, liver, spleen, lung, and kidney, were collected, homogenized in PBS using a high-throughput tissue grinder, serially diluted, and spread onto LB agar plates for bacterial colony counting.

2.18. Evaluation of the efficacy of treatment with intratumoral bacteria

Treatment was initiated on the second day after bacterial injection, when the tumor volume reached approximately 100 mm^3 and the intratumoral bacteria-colonized model had been established. The mice were randomly divided into four groups (n = 5 per group): Control (PBS), Tob–SS–Tob NPs (10 mg/kg), Gm–SS–Gm NPs (10 mg/kg), and Tob–SS–Gm NPs (10 mg/kg). The formulations were administered every 2 days for 14 days. During treatment, body weight and tumor volume were monitored. Tumor volume was calculated using the formula: tumor length × tumor width^2/2. Relative tumor volume was expressed as V/V_0, where V_0 represents the initial tumor volume on day 0. For animal welfare reasons, mice were euthanized when the tumor volume exceeded 1500 mm^3.

To quantify intratumoral bacterial burden, tumors were excised, homogenized using a high-throughput tissue grinder, diluted with PBS, spread onto agar plates, and photographed after 24 h of culture. Tumor tissues, lymph nodes (LNs), and spleens were collected and processed into single-cell suspensions, which were then filtered through a 70 μm cell strainer. The cells were stained with PerCP/Cyanine5.5 anti-mouse CD45, PE anti-mouse CD3, FITC anti-mouse CD4, APC anti-mouse CD8a, FITC anti-mouse/human CD11b, PE anti-mouse F4/80, APC anti-mouse CD86, Brilliant Violet 421 anti-mouse CD206 (MMR), PE anti-mouse CD11c, and FITC anti-mouse CD80, followed by flow-cytometric analysis. In addition, blood samples were collected and centrifuged at 3500 rpm for 10 min to obtain serum, and the concentrations of IL-6 and IFN-γ were measured using ELISA kits.

2.19. Statistical analysis

All quantitative data are presented as mean ± standard deviation (SD). Statistical analyses were performed using Student's t-test for comparisons between two groups and one-way analysis of variance (ANOVA) for comparisons among multiple groups. A value of $p < 0.05$ was considered statistically significant. Statistical significance is indicated as follows: $p < 0.05$, $p < 0.01$, $p < 0.001$, and $p < 0.0001$.

3. Results and discussion

3.1. Synthesis and Characterization of Tob–SS–Gm NPs

The synthetic routes and procedures for the Tob–SS–Gm molecule via disulfide bonding are illustrated in Fig. S1 (Supporting Information). First, a disulfide intermediate containing Tob (designated Tob-DDA) was synthesized via an esterification reaction with 3,3′-dithiodipropionic acid (DDA). Subsequently, further esterification of Tob-DDA with Gm was performed to obtain the dimeric Tob–SS–Gm molecule. For comparison, Gm–SS–Gm (Fig. S2, Supporting Information) and Tob–SS–Tob (Fig. S3, Supporting Information) were also synthesized with similar protocols. The synthesized AiDCs were self-assembled into nanoparticles via a two-phase interface method (Tob–SS–Gm NPs, Gm–SS–Gm NPs, and Tob–SS–Tob NPs) (Fig. 1A). Tob–SS–Gm NPs are formed by the self-assembly of the covalently conjugated prodrug Tob–SS–Gm, in which Tob and Gm are linked at a defined molar ratio of 1:1. Based on the molecular weight of the conjugate (929.97 g/mol), the theoretical drug content corresponds to 0.503 mg Tob and 0.283 mg Gm per mg NPs, equivalent to 1.075 μmol Tob and 1.075 μmol Gm per mg NPs. The theoretical drug composition of Tob–SS–Gm NPs is summarized in Table S1, Supporting Information. Subsequently, the chemical structures of Tob–SS–Gm, Tob–SS–Tob, and Gm–SS–Gm were systematically evaluated using ^{1}H NMR, FTIR, and UV-vis absorption spectroscopy. As shown in Fig. 1B, Fig. S4-6, Supporting Information, the characteristic carboxyl proton signal (-COOH) of DDA at 12.36 ppm disappears in the Tob–SS–Gm spectrum, indicating a successful esterification reaction. In addition, the characteristic disulfide bond (-S-S-) signals at 2.60-2.62 ppm and 2.87-2.90 ppm appeared for Tob–SS–Gm. In FTIR spectra (Fig. 1C), a distinct carbonyl stretching vibration of the ester bond is observed in the 1740-1650 cm^{-1} range, and a characteristic disulfide absorption peak appears at 450-500 cm^{-1}, confirming the dynamic conjugation of Tob–SS–Gm via the disulfide bond. Additionally, the UV-vis absorption spectra (Fig. 1D) of Tob–SS–Gm and Gm–SS–Gm exhibit a red-shifted absorption peak (a characteristic absorption peak at 268 nm for Gm), further confirming the successful synthesis of these binary AiDCs molecules. Their morphology and particle size were characterized by scanning electron microscopy (SEM), transmission electron microscopy (TEM), and dynamic light scattering (DLS). As shown in Fig. 1E and F, Tob–SS–Gm NPs exhibit a rice-like structure with an average diameter of 253 ± 6.8 nm. For comparison, Gm–SS–Gm NPs and Tob–SS–Tob NPs present homogenous spherical morphology with an average diameter of 168.1 ± 17.4 nm and 240.1 ± 11.5 nm, respectively (Fig. S7, Supporting Information). The zeta potentials of Tob–SS–Gm NPs, Tob–SS–Tob NPs, and Gm–SS–Gm NPs were further measured by DLS, and all nanoparticles exhibited negative surface charges (Fig. S8, Supporting Information), suggesting good colloidal stability in physiological environments. Meanwhile, a pronounced Tyndall effect was observed for the Tob–SS–Gm NPs suspension, indicating excellent colloidal dispersion and self-assembly capability. Stability assessments under simulated physiological conditions (PBS, 37°C) and serum-containing conditions (PBS + 10% FBS, 37°C) showed that nanoparticle size remained stable over 5 days (Fig. 1G, Fig. S9, Supporting Information), confirming their physiological stability.

Considering the dynamic disulfide bonding of the linker, the GSH-responsive performance of the AiDCs was evaluated. DLS analysis showed that after co-incubation with GSH, Tob–SS–Gm NPs exhibited a

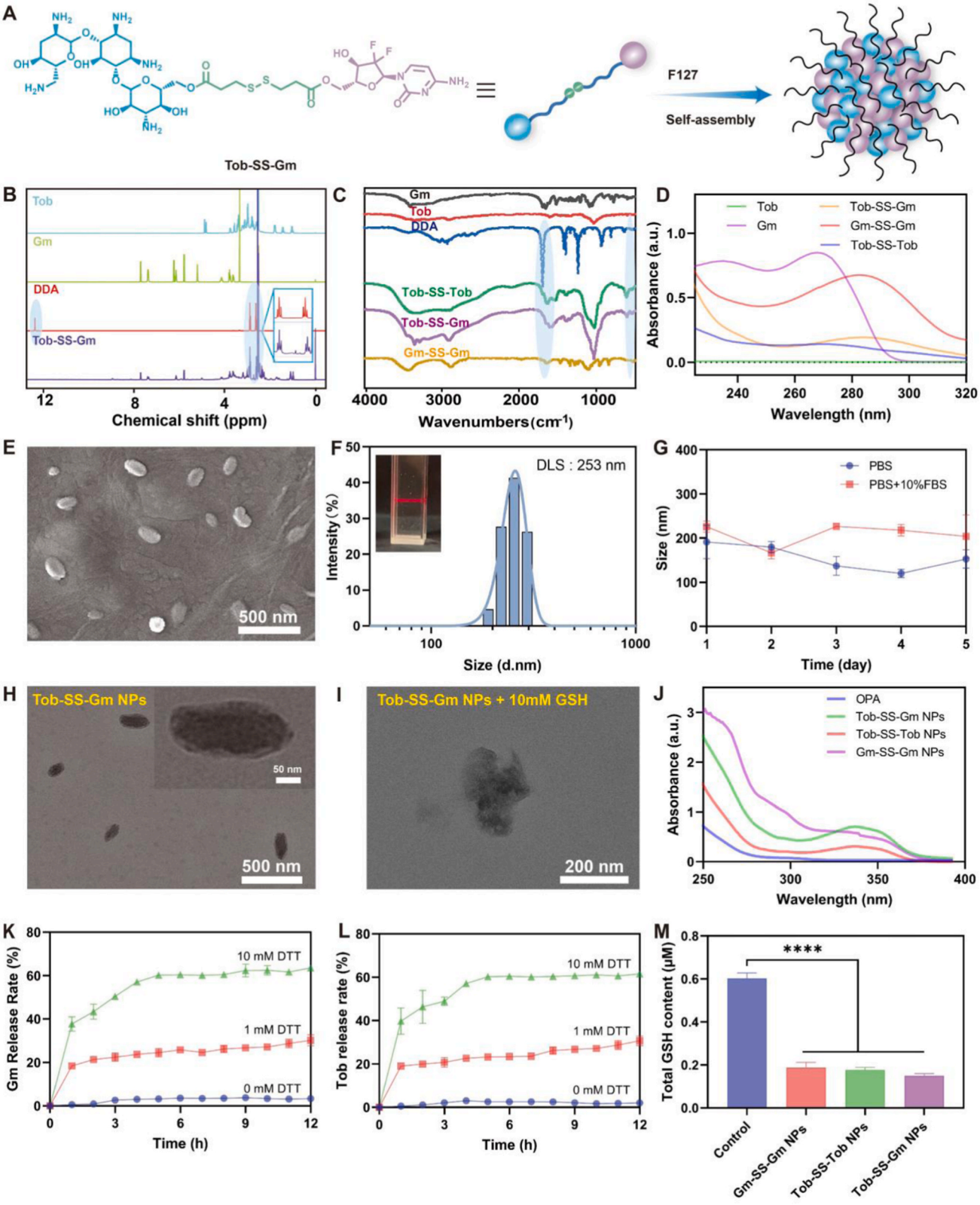


Fig. 1. Characterization of Tob–SS–Gm NPs. (A) Schematic diagram of preparing Tob–SS–Gm NPs. (B) ^{1}H NMR spectra of Tob, Gm, DDA, and Tob–SS–Gm in DMSO-d_6. (C) FTIR spectra of Tob, Gm, DDA, Tob–SS–Tob, Gm–SS–Gm, and Tob–SS–Gm. (D) UV-vis absorption spectra of Tob, Gm, DDA, Tob–SS–Tob, Gm–SS–Gm, and Tob–SS–Gm. (E) Scanning electron microscopy (SEM) image of Tob–SS–Gm NPs. (F) Hydrodynamic size distribution of Tob–SS–Gm NPs measured by dynamic light scattering (DLS). (G) Particle size stability of Tob–SS–Gm NPs in different buffer solutions over 5 days. (H&I) Transmission electron microscopy (TEM) image of Tob–SS–Gm NPs with or without incubation with 10 mM GSH. (J) UV-vis absorption spectra of Tob–SS–Gm NPs, Tob–SS–Tob NPs, and Gm–SS–Gm NPs in the presence of DTT and OPA. The peak at 338 nm indicates the formation of OPA–thiol adducts derived from thiol groups generated by disulfide bond cleavage. (K&L) Accumulative release profiles of Gm and Tob from Tob–SS–Gm NPs under different GSH conditions (0, 1, and 10 mM). (M) Intracellular GSH level of Panc02 cell after incubation with Gm–SS–Gm NPs, Tob–SS–Tob NPs, and Tob–SS–Gm NPs for 24 h.

bimodal size distribution, suggesting the cleavage of disulfide bonds and the subsequent disintegration of the nanoparticle structure (Fig. S10, Supporting Information). Meanwhile, the morphology of Tob–SS–Gm NPs was significantly disrupted after co-incubation with 10 mM GSH solution (Fig. 1H and I), further confirming the reduction-responsive structural instability under a high-GSH environment. To further verify the cleavage behavior using UV-vis spectroscopy, OPA was employed as a colorimetric reagent [29]. However, no obvious signal was detected, likely due to side reactions between the amino groups of GSH and OPA, which interfered with the accurate detection of thiol groups. To circumvent this issue, dithiothreitol (DTT), which contains thiol groups but lacks amino groups, was selected as a substitute for GSH. Both GSH and DTT are widely used as reducing agents in disulfide-based nanomedicine to simulate reductive environments for evaluating disulfide bond cleavage *in vitro* [36,37]. After incubating with DTT and OPA, Tob–SS–Gm NPs, Tob–SS–Tob NPs, and Gm–SS–Gm NPs solutions presented a distinct UV absorption peak at 338 nm (Fig. 1J), confirming that the disulfide bonds in AiDCs could be reduced and cleaved under a high GSH microenvironment. Following the same protocol, *in vitro* drug release behaviors were performed in buffered solutions simulating physiological conditions (PBS, pH 7.4) and tumor microenvironment (1 and 10 mM GSH in PBS) (Fig. 1k and L). Under physiological conditions, only 1.91% and 2.92% of Tob and Gm were released after 12 h, respectively, confirming the high structural stability of Tob–SS–Gm NPs. However, the 12-h release amount increased markedly to 30.70% (Tob) and 31.99% (Gm) under 1 mM GSH conditions. Furthermore, higher release amounts of 60.94% (Tob) and 63.62% (Gm) were detected under a 10 mM GSH environment, demonstrating rapid nanoparticle disassembly and drug release. Besides, the intracellular GSH levels of Panc02 cells after treatment with the three AiDCs decreased significantly compared to the control group (Fig. 1M), indicating intracellular redox consumption, which is consistent with disulfide cleavage and drug release of the two drugs in living cells.

3.2. *In vitro antibacterial performance*

The *in vitro* antibacterial activity of Tob–SS–Gm NPs was systematically evaluated in comparison with free Tob and Tob–SS–Tob NPs. The minimum inhibitory concentration (MIC) and minimum bactericidal concentration (MBC) against *Escherichia coli Nissle 1917* (*E. coli*) and *Staphylococcus aureus* (*S. aureus*) were first determined. As shown in Fig. 2A and B, Fig. S11, Table S2, Supporting Information, free Tob displayed MIC and MBC values of 1 μg/mL (2.14 μM) and 2 μg/mL (4.28 μM), respectively. In comparison, Tob–SS–Gm NPs showed MIC and MBC values of 8 μg/mL (3.52 μM) and 16 μg/mL (7.04 μM), while Tob–SS–Tob NPs displayed MIC and MBC values of 8 μg/mL (4.31 μM) and 16 μg/mL (8.62 μM) against both *E. coli* and *S. aureus*. Although higher MIC/MBC values were observed on a mass concentration basis, the antibacterial activity remains comparable when normalized to the molar concentration of Tob, indicating that the intrinsic antibacterial function of Tob is largely preserved after conjugation and nanoparticle formation. Further antibacterial testing against *E. coli* was conducted by monitoring the bacterial growth curve at the MIC of Tob–SS–Gm NPs (Fig. S12, Supporting Information). The results indicate that Tob–SS–Gm NPs effectively suppress the growth of *E. coli* during 12 h incubation, confirming effective bacterial growth inhibition. In addition, agar diffusion assays (Fig. 2C) show that all AiDCs treatment groups generate inhibition zones of comparable diameters, indicating comparable antibacterial potency under diffusion conditions [38]. To directly visualize bacterial viability, confocal laser scanning microscopy (CLSM) combined with live/dead staining (Fig. 2D) reveals predominantly green fluorescence (live bacteria) in the control group, whereas AiDCs-treated groups displayed significantly diminished green fluorescence, indicating significant bacterial killing. SEM images (Fig. 2E, Fig. S13, Supporting Information) further show AiDCs-treated bacteria exhibited severe structural damage (including membrane collapse and irregular surface pores) while untreated bacteria retained intact morphology.

To directly assess the interaction between bacteria and Tob–SS–Gm NPs, a colocalization experiment was conducted using Nile Red (NR)-labeled NR@Tob–SS–Gm NPs. The confocal images (Fig. 2F, Fig. S14, Supporting Information) show clear colocalization of green and red fluorescence, indicating the efficient bacterial targeting capability of Tob–SS–Gm NPs. Motivated by the nanostructure-mediated targeting performance, the antibacterial activity of different nanoparticles was further evaluated by crystal violet staining. As shown in Fig. 2G and H, all Tob groups significantly reduced biofilm biomass compared to the PBS group. No statistically significant differences were observed among free Tob, Tob–SS–Tob NPs, and Tob–SS–Gm NPs, indicating comparable antibiofilm efficacy [39,40]. This further confirms that Tob is the primary contributor to antibacterial and antibiofilm activity, while Gm does not play a significant role in this context. [41]. Notably, these experiments were conducted in the absence of exogenous GSH, indicating that the observed antibacterial effects are primarily attributed to the intrinsic activity rather than GSH-triggered drug release.

3.3. *In vitro antitumor efficacy*

After confirming the excellent antibacterial properties of Tob–SS–Gm NPs, further antitumor evaluations were performed to comprehensively assess the therapeutic potential of AiDCs as an antitumor platform. Initially, the CCK-8 assay was employed to evaluate the *in vitro* cytotoxicity of different AiDCs on Panc02 cells and L929 cells. The results showed that free Gm, Gm–SS–Gm NPs, and Tob–SS–Gm NPs exhibited dose-dependent *in vitro* cytotoxicity, indicating the retained antitumor activity after conjugation. In contrast, Tob–SS–Tob NPs demonstrated minimal cytotoxicity toward Panc02 cells (Fig. 3A), supporting the notion that antitumor effect of these AiDCs is primarily contributed by the Gm component. Notably, compared to free Gm, both Gm–SS–Gm NPs and Tob–SS–Gm NPs showed significantly reduced cytotoxicity toward L929 cells, highlighting their improved biosafety (Fig. 3B). Specifically, when the concentration was lowered to 12 μg/mL, the viability of Panc02 cells was approximately 50%, while that of L929 cells was as high as 90%. These data suggest that Tob–SS–Gm NPs exhibit preferential cytotoxicity toward Panc02 cells with relatively lower cytotoxicity toward L929 cells under the present *in vitro* conditions. Based on these findings, a Gm concentration of 12 μg/mL was selected as the reference condition (Table S3, Supporting Information), and the concentrations of all nanoparticles were adjusted to maintain molar concentrations of Gm in subsequent experiments. Further hemolysis assays were performed to evaluate the blood compatibility *in vitro* (Fig. 3C). It is clear that even under a high concentration of 1 mg/mL, Tob–SS–Gm NPs show a low hemolysis rate below 2%, which is within the acceptable safety threshold. These results indicate that Tob–SS–Gm NPs possess promising *in vitro* antitumor activity with acceptable biocompatibility.

Subsequently, Annexin V-FITC/PI double staining combined with flow cytometry was employed for quantitative analysis of cell apoptosis (Fig. 3D and E). Compared to the control group, both Gm–SS–Gm NPs and Tob–SS–Gm NPs significantly induce apoptosis in Panc02 cells, with apoptosis rates of 35.7% and 38.1%, respectively. The viability of Panc02 cells in each treatment group was further visualized by CLSM (Fig. 3F and G). Cells in both the control and Tob–SS–Tob NPs groups predominantly exhibited strong and dense green fluorescence, indicating high viability. In contrast, reduced green fluorescence and increased red fluorescence were observed in the Gm–SS–Gm NPs and Tob–SS–Gm NPs groups, suggesting enhanced cytotoxic effects. To further evaluate whether the covalent conjugation strategy provides additional benefits over conventional combination therapy, a physical mixture of free Tob and free Gm was included as a control (Fig. S15, Supporting Information). The free drug combination exhibited comparable cytotoxic effects to Tob–SS–Gm NPs under bacteria-free conditions, indicating that the observed tumor cell killing is primarily

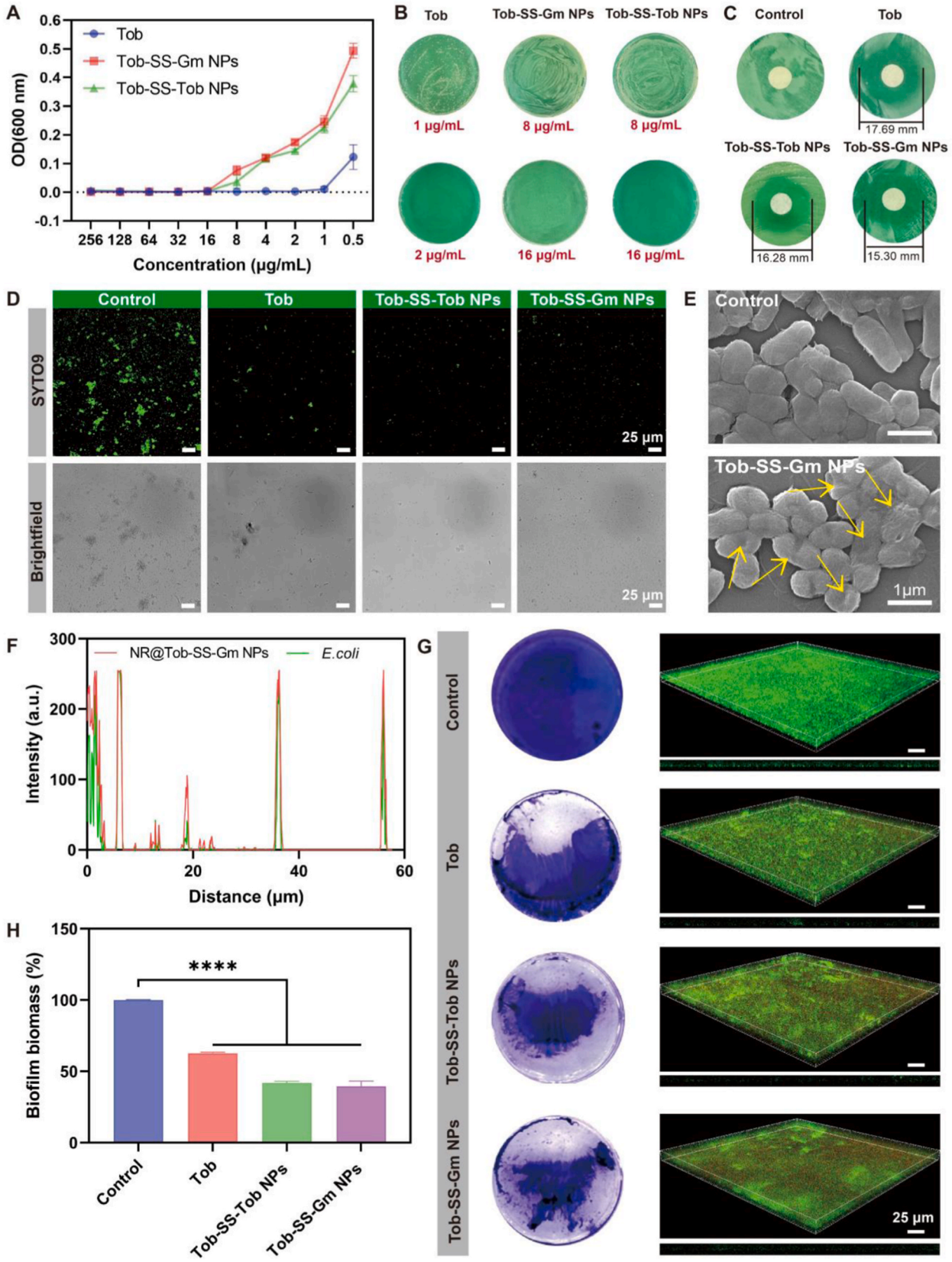


Fig. 2. *In vitro* antibacterial activity evaluation. (A&B) Minimum inhibitory concentration (MIC) and minimum bactericidal concentration (MBC) of Tob, Tob–SS–Tob NPs, and Tob–SS–Gm NPs against *E. coli* after 24 h incubation. (C) Agar diffusion assay of Tob, Tob–SS–Tob NPs, and Tob–SS–Gm NPs against *E. coli* after 24 h incubation. (D) Confocal laser scanning microscopy (CLSM) images of *E. coli* after treatment with Tob, Tob–SS–Tob NPs, and Tob–SS–Gm NPs. (E) Scanning electron microscopy (SEM) images of *E. coli* with/without treatment with Tob–SS–Gm NPs. (F) The linear colocalization analysis of *E. coli* with NR@Tob–SS–Gm NPs. (G) Crystal violet staining and CLSM images of *E. coli* biofilms after treatment with Tob, Tob–SS–Tob NPs, and Tob–SS–Gm NPs. (H) Quantitative analysis of biofilm biomass after various treatments. (For interpretation of the references to color in this figure legend, the reader is referred to the Web version of this article.)

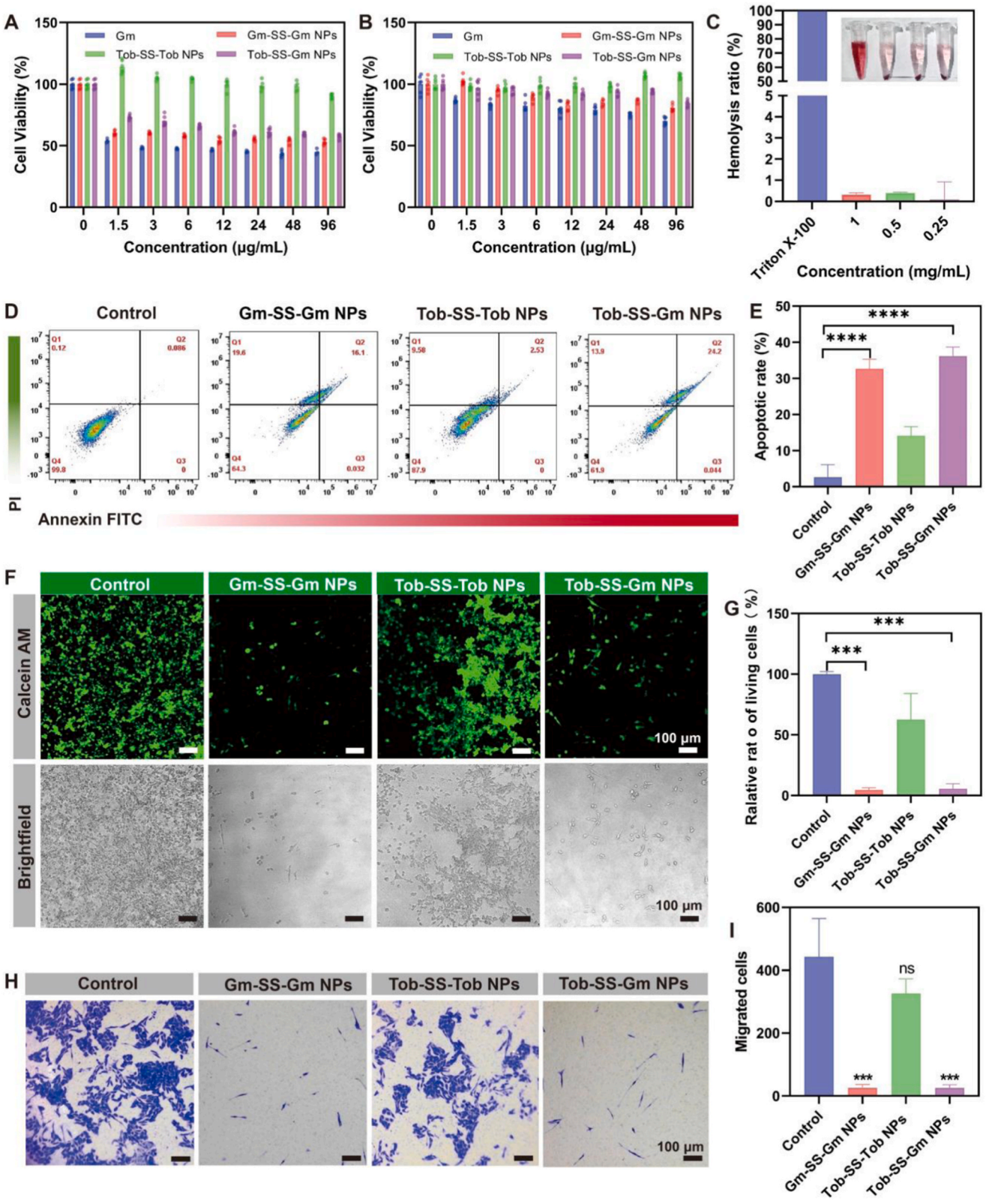


Fig. 3. *In vitro* antitumor efficacy and biosafety evaluation. (A) Relative cell viability of Panc02 cells after treatment with various concentrations of Gm, Gm–SS–Gm NPs, Tob–SS–Tob NPs, and Tob–SS–Gm NPs. (B) Relative cell viability of L929 cells after treatment with various concentrations of Gm, Gm–SS–Gm NPs, Tob–SS–Tob NPs, and Tob–SS–Gm NPs. (C) Hemolysis rate of Triton X-100 and Tob–SS–Gm NPs at different concentrations (0.25, 0.5, and 1 mg/mL) using mouse whole blood. (D&E) Apoptosis analysis of Panc02 cells after treatment with Gm–SS–Gm NPs, Tob–SS–Tob NPs, and Tob–SS–Gm NPs. (F&G) Fluorescence microscopy images of Panc02 cells after treatment with Gm–SS–Gm NPs, Tob–SS–Tob NPs, and Tob–SS–Gm NPs, and then stained with Calcein-AM. (H&I) Cell migration assays of Panc02 cells after treatment with Gm–SS–Gm NPs, Tob–SS–Tob NPs, and Tob–SS–Gm NPs.

associated with the chemotherapeutic activity of Gm. To further evaluate the inhibitory effect on the metastatic potential of pancreatic cancer, a Transwell migration assay was performed. As shown in Fig. 3H and I, the control group shows strong migratory capability, with an average of more than 400 migrated cells. In contrast, Gm–SS–Gm NPs and Tob–SS–Gm NPs treatment significantly suppress Panc02 cell migration, reducing the number of migrated cells by approximately 20-fold compared to the control. These findings suggest that Tob–SS–Gm NPs suppress tumor-cell migratory behavior *in vitro*.

3.4. Intratumoral bacteria eliminating enhanced chemotherapy

Inspired by the excellent antibacterial and chemotherapeutic activities of Tob–SS–Gm NPs, an *E. coli* colonization tumor model was established based on Panc02 cells to evaluate the intratumoral bacteria eliminating enhanced chemotherapy performance [13,14]. Specifically, Panc02 cells in the exponential growth phase were infected with *E. coli* at a bacterial-to-cell ratio of 10:1 to create a stable intracellular infection model (Fig. 4A). Subsequently, cells were treated with Gm, Tob, Tob–SS–Tob NPs, Gm–SS–Gm NPs, and Tob–SS–Gm NPs and a physical mixture of Gm + Tob for 24 h. After lysis with 0.1% Triton X-100, intracellular bacteria were collected and plated for colony enumeration. As shown in Fig. 4B, Fig. S16, Supporting Information, colony counts were markedly reduced in the Tob, Tob–SS–Tob NPs, Tob–SS–Gm NPs, and Gm + Tob groups, whereas Gm and Gm–SS–Gm NPs showed no significant decrease compared to the control group. These results indicate that antibacterial activity is primarily associated with the presence of Tob. Quantitative analysis (Fig. 4C) reveals that Tob–SS–Gm NPs achieved an approximate 4 $\log_{10}$ CFU intracellular *E. coli* compared to the untreated control. Collectively, these findings suggest that both the conjugated nanodrug and the free drug combination effectively reduce intracellular bacterial burden, which may contribute to the enhanced therapeutic response observed under bacteria-colonized conditions. Furthermore, Annexin V-FITC/PI staining coupled with flow cytometry was employed to explore the relationship between intracellular bacterial clearance and tumor cell apoptosis (Fig. 4D, Fig. S17, Supporting Information). The apoptosis rate was 43.2% for the Gm–SS–Gm NPs group, 25.6% for the Tob–SS–Tob NPs group, and 53.7% for the Tob–SS–Gm NPs group. Notably, Tob–SS–Gm NPs induced a higher apoptosis rate than Gm–SS–Gm NPs in bacteria-colonized Panc02 cells. This enhanced effect may be attributed to the antibacterial activity of Tob, which may reduce intracellular bacterial burden and thereby alleviate bacteria-mediated Gm inactivation. Consequently, the elimination of intratumoral bacteria may partially restore the chemotherapeutic efficacy of Gm in bacteria-colonized Panc02 cells. Consistently, the free Tob + Gm also exhibited increased cytotoxicity in bacteria-colonized conditions (Fig. S18, Supporting Information), supporting the notion that bacterial presence influences the therapeutic response. However, the covalent conjugation strategy may provide additional benefits in terms of coordinated delivery and redox-responsive drug release. The apoptotic trends were further validated by CLSM imaging (Fig. 4E and F). These results support the concept of antibacterial-assisted Gm chemotherapy based on the AiDC design.

Given that conventional two-dimensional culture systems fail to accurately model the complex three-dimensional tumor tissues *in vivo*, a 3D tumor spheroid model was employed to evaluate the penetration and inhibitory performances of Tob–SS–Gm NPs[38,42–44]. Visualization was performed using bright-field imaging together with Calcein AM staining (Fig. 4G, Fig. S19, Supporting Information). Tumor spheroids in the control group retained intact and compact structures, which is indicative of optimal cellular viability. In contrast, all drug-treated groups exhibited reduced spheroid density and impaired structural integrity. Among these treatment groups, Tob–SS–Gm NPs treatment shows the most loosely organized structure and lowest cell density, indicating the most pronounced antitumor effect. Collectively, these findings not only confirm the excellent penetration capacity of Tob–SS–Gm NPs in three-dimensional tumor tissues but also highlight the antibacterial-enhanced chemotherapy effects. To further evaluate the effect of the nanoparticles on tumor cell migration, a scratch wound healing assay was additionally performed. As shown in Fig. S20, Supporting Information, under sterile conditions, all treatments exhibited moderate inhibition of Panc02 cell migration compared with the control group. Notably, in co-culture with *E. coli*, the migratory capacity of Panc02 cells was markedly enhanced, as evidenced by accelerated wound closure in the control group (Fig. S21, Supporting Information), suggesting a bacteria-associated pro-migratory effect.

Following treatment, nanoparticle formulations effectively suppressed bacteria-induced cell migration to varying degrees. Among them, Tob–SS–Gm NPs exhibited the strongest inhibitory effect on wound closure. These findings indicate that the nanoparticles can effectively attenuate bacteria-associated tumor cell motility. Furthermore, a Transwell invasion assay was performed to evaluate the inhibitory effect of the nanoparticles on tumor invasive behavior. As shown in Fig. S22, Supporting Information, co-culture with *E. coli* significantly enhanced the invasive capacity of Panc02 cells, whereas all treatment groups effectively reduced cell invasion through the membrane. These findings are consistent with the scratch wound healing results, further demonstrating that Tob–SS–Gm NPs can effectively inhibit bacteria-associated tumor cell migration and invasion.

3.5. Cellular uptake, in vivo biodistribution and bacterial colonization ability

To assess the tumor-targeting ability of Tob–SS–Gm NPs *in vivo*, the *in vitro* cellular uptake was first investigated. C6-loaded Tob–SS–Gm NPs (denoted C6@Tob–SS–Gm NPs) were prepared and co-incubated with Panc02 cells for different times (Fig. 5A, Fig. S23, Supporting Information). The CLSM images show a time-dependent increase in intracellular green fluorescence intensity in cells treated with C6@Tob–SS–Gm NPs. In contrast, the fluorescence signal in the free C6 group gradually decreased and was barely detectable after 24 h incubation, indicating that the self-assembled nanostructure of AiDCs facilitates efficient cellular internalization. Furthermore, the tissue penetration capability was evaluated using the three-dimensional tumor spheroid model. As shown in Fig. 5B, NR@Tob–SS–Gm NPs effectively penetrate deeply into the core region of the spheroids, suggesting their potential to achieve efficient delivery to cells within dense tumor tissues. To further validate the *in vivo* biodistribution and tumor-targeting capability, Tob–SS–Gm NPs were labeled with Cy7 dye (Cy7@Tob–SS–Gm NPs) and then administered via tail vein injection to subcutaneous Panc02 tumor-bearing mice. The *in vivo* fluorescence images reveal that Cy7@Tob–SS–Gm NPs gradually accumulate in the tumor site, with the highest fluorescence intensity at 6 h post-injection (Fig. 5C and D). This dynamic distribution suggests that Tob–SS–Gm NPs exhibit good stability in systemic blood circulation and effective targeting ability to tumor tissues via the enhanced permeability and retention (EPR) effect[45–47]. Furthermore, 12 h post-administration, major organs, including heart, liver, spleen, lung, and kidney, alongside tumor tissues, were excised for fluorescence imaging analysis (Fig. 5E, Fig. S24, Supporting Information). Cy7@Tob–SS–Gm NPs exhibited relatively stronger fluorescence signals in tumor tissues compared with major organs such as liver and kidney, suggesting preferential tumor accumulation. This distribution pattern is consistent with passive tumor targeting mediated by the EPR effect rather than active targeting. These results demonstrate that Tob–SS–Gm NPs possess pronounced tumor tissue selectivity, which enables efficient tumor accumulation under systemic administration and enhanced therapeutic efficacy.

Besides, before evaluating the *in vivo* therapeutic efficacy of AiDCs based on an “antibacterial-enhanced chemotherapy” strategy, an intratumoral bacteria-colonized Panc02 tumor model was constructed according to our previous study [13]. After *i.v.* injection, the bacterial burdens in tumor tissues and major organs were systematically assessed

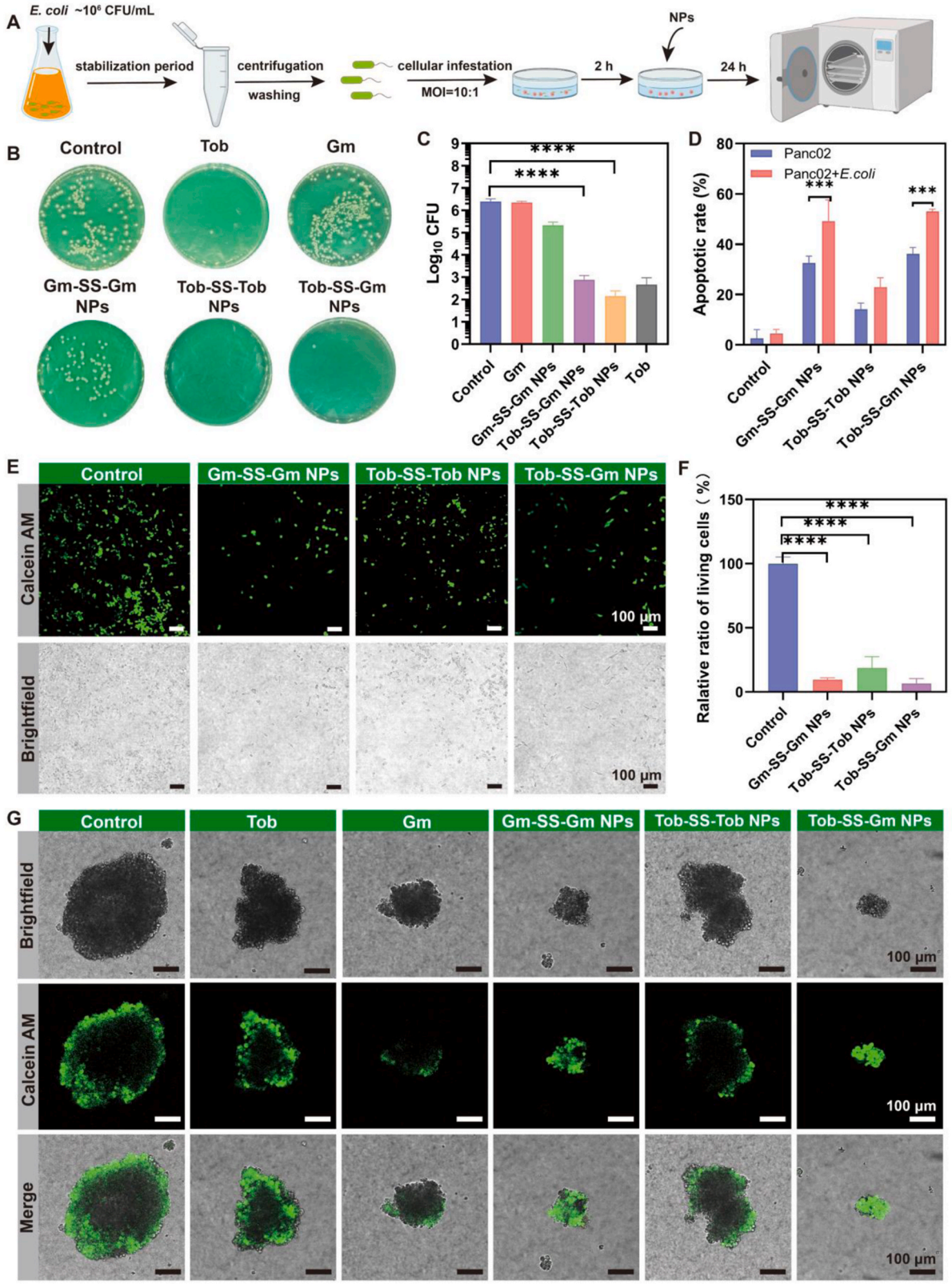


Fig. 4. *In vitro* antibacterial-enhanced chemotherapy in an intratumoral bacteria-colonized tumor model. (A) Schematic illustration of the *in vitro* intratumoral bacteria-colonized tumor model and therapeutic protocols. (B&C) Colony-forming units (CFU) of residual intratumoral bacteria after treatment with various formulations. (D) Quantitative analysis of apoptosis rates in normal Panc02 cells and intratumoral *E. coli*-colonized Panc02 cells after treatment with various formulations. (E&F) Fluorescence images and corresponding quantitative analysis of intratumoral *E. coli*-colonized Panc02 cells after treatment with Tob–SS–Tob NPs, Gm–SS–Gm NPs, and Tob–SS–Gm NPs (12 μg/mL). (G) Fluorescence images of three-dimensional (3D) tumor spheroids after treatment with various formulations.

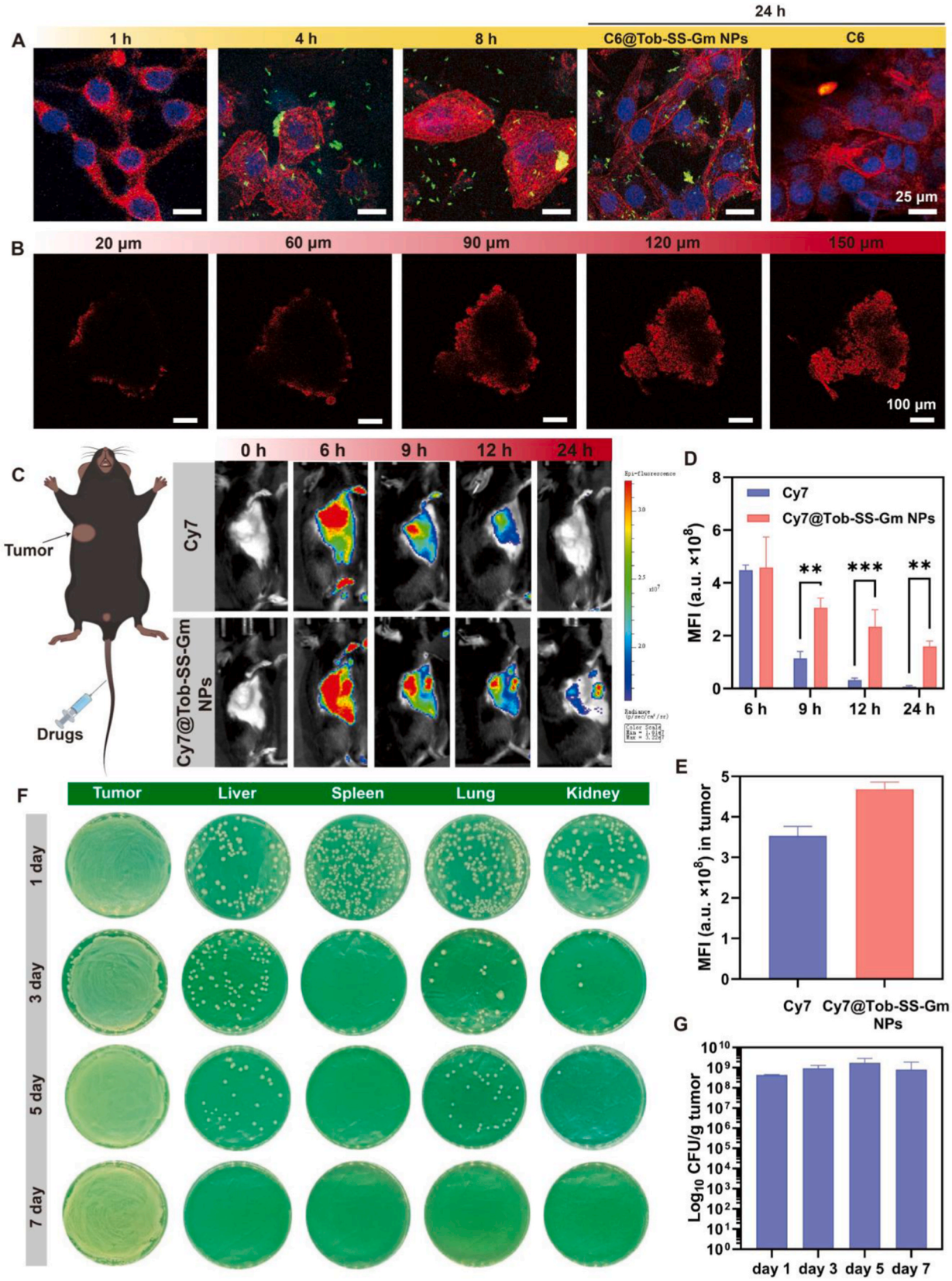


Fig. 5. Evaluation of the targeting ability of Tob–SS–Gm NPs and *in vivo* bacterial colonization. (A) Fluorescence images of Panc02 cells after co-incubation with C6@Tob–SS–Gm NPs or free C6 for 1, 4, 8, and 24 h. (B) Fluorescence images of three-dimensional (3D) Panc02 tumor spheroids after co-incubation with NR@Tob–SS–Gm NPs for 24 h at different Z-axis depths. (C) *In vivo* biodistribution of Cy7@Tob–SS–Gm NPs and free Cy7 in Panc02 tumor-bearing mice after *intravenous (i.v.)* injection. (D) Fluorescence intensity of tumor regions at different time points after *i.v.* injection. (E) *Ex vivo* analysis of fluorescence intensity in tumor tissues 12 h post-injection of Cy7@Tob–SS–Gm NPs and free Cy7. (F&G) Bacterial colonization in major organs and tumors of mice at different time points after *i.v.* injection.

by CFU counting at multiple time points (days 1, 3, 5, and 7). The images revealed that CFU levels in tumor tissues were consistently and significantly higher than those in the liver, spleen, lung, and kidney (Fig. 5F and G), indicating that the tumor microenvironment provides favorable conditions for colonization and survival of exogenous bacteria. Notably, the bacterial load within tumors remained relatively stable over the 7-day observation period, with no significant fluctuations observed. This finding suggests that bacteria can establish a dynamic equilibrium within this tumor niche and exhibit the capacity for long-term survival. In contrast, bacterial counts in normal organs remained consistently low, with no detectable colonization by day 7, which implies that these tissues collectively limit bacterial colonization and proliferation of *E. coli*. Taken together, these findings lay a solid foundation for the development of therapeutic strategies aimed at enhancing chemotherapy sensitivity through the eradication of intratumoral bacteria.

3.6. *In vivo biosafety and antitumor evaluation*

Motivated by the excellent tumor-targeting and enrichment capabilities, further *in vivo* safety evaluations were conducted to support subsequent antitumor therapy. Healthy C57BL/6 mice were administered with Tob–SS–Gm NPs (2 mg/mL and 10 mg/mL) via *i.v.* injection every two days for 14 total days. The blood was collected for serum biochemical analysis to evaluate the *in vivo* biosafety of Tob–SS–Gm NPs. As shown in Fig. S25, Supporting Information, no significant difference in alanine aminotransferase (ALT), aspartate aminotransferase (AST), and alkaline phosphatase (ALP) levels was detected for high concentration Tob–SS–Gm NPs-treated mice compared to the PBS-treated mice, indicating no toxicity to the liver. Meanwhile, the normal level of uric acid (UA) and urea displays healthy kidney function, verifying the excellent *in vivo* biocompatibility.

Subsequently, a subcutaneous intratumoral bacteria-colonized pancreatic cancer model was established using Panc02 cells to systematically evaluate *in vivo* antitumor efficacy (Fig. 6A). The tumor-bearing mice were randomly divided into four groups (n = 5) as follows: G1) PBS, G2) Tob–SS–Tob NPs, G3) Gm–SS–Gm NPs, and G4) Tob–SS–Gm NPs. During the therapeutic procedure, mice were i.v. injected with 100 μL PBS, Tob–SS–Tob NPs, Gm–SS–Gm NPs, and Tob–SS–Gm NPs (10 mg/kg) every two days. The body weights of mice in each group were continuously monitored. The results show stable and gradually increased body weights of mice in all groups (Fig. 6B), indicating good systemic tolerance to the administered formulations. Meanwhile, the hematoxylin and eosin (H&E) staining of major organs (heart, liver, spleen, lung, and kidney) revealed no apparent histopathological abnormalities in treated groups compared with the control group (Fig. S26, Supporting Information), further confirming *in vivo* biosafety. Tumor volume changes were direct indicators of antitumor efficacy (Fig. 6C, Fig. S27, Supporting Information). Compared with the PBS group, Tob–SS–Tob NPs (G2) exhibited only limited tumor growth inhibition, which may be attributed to the elimination of intratumoral bacteria without direct chemotherapeutic activity. In contrast, Gm–SS–Gm NPs (G3) significantly suppressed tumor growth, consistent with the *in vitro* cytotoxicity results. Notably, the Tob–SS–Gm NPs group (G4) showed the overall best therapeutic trend within the current observation window (Fig. 6D). Although the difference in tumor growth inhibition between G3 and G4 was moderate within the current observation period, Tob–SS–Gm NPs still exhibited a trend toward enhanced therapeutic efficacy. This effect may be associated with simultaneous bacterial clearance and chemotherapy, which together could enhance tumor sensitivity to treatment under bacteria-colonized conditions. The final tumor volume in the G4 group was reduced to approximately 41.7% of that in the PBS group and was markedly lower than that in the Gm–SS–Gm NPs group. Consistently, the relative tumor weight in the G4 group was also significantly decreased, reaching approximately 55% of that in the PBS group (Fig. S28, Supporting Information), further confirming the therapeutic advantage of the antibacterial-enhanced chemotherapy strategy. To visualize the bacterial status, colony counts (Fig. 6E, Fig. S29, Supporting Information) were employed using the tumor tissues, and it reveals a significant reduction in bacterial burden in the Tob–SS–Gm NPs group compared to the Gm–SS–Gm NPs group, indicating efficient intratumoral bacterial eradication by AiDCs. This reduction may effectively alleviate bacteria-associated Gm inactivation and resistance, thereby enhancing tumor chemosensitivity.

As intratumoral bacteria can modulate the host inflammatory environment, interleukin (IL)-6 and interferon (IFN)-γ in serum were detected. As shown in Fig. 6F, the Tob–SS–Gm NPs group exhibited a markedly elevated expression of IL-6, which was 3.4-fold higher than that in the control group. Meanwhile, a significant increase was observed in the Tob–SS–Gm NPs group compared to the Gm–SS–Gm NPs group, suggesting that bacterial elimination is associated with enhanced inflammatory signaling. Additionally, the antitumor immune cytokine IFN-γ was significantly upregulated in the G4 group: its expression was 7.33-fold higher than the control level, and this increase exceeded the 2.37-fold and 5.26-fold elevations observed in the Tob–SS–Tob NPs and Gm–SS–Gm NPs groups, respectively (Fig. 6G). Furthermore, H&E, TUNEL, and Ki-67 staining were performed on tumor tissues from each group to further evaluate antitumor effects. H&E staining revealed a pronounced reduction in tumor cell density in the Tob–SS–Gm NPs group compared with the other treatment groups (Fig. 6H). Consistently, enhanced apoptotic signals were observed by TUNEL staining (Fig. 6I), accompanied by a marked decrease in Ki-67–positive proliferating cells (Fig. 6J). All above findings demonstrate that intratumoral bacterial elimination by Tob–SS–Gm NPs could effectively enhance the efficacy of chemotherapy for pancreatic cancer.

3.7. *In vivo antitumor immune response via DAMPs*

To evaluate changes in intratumoral *E. coli* colonization after different treatments, Gram staining of tumor sections was performed. As shown in Fig. 7A, tumors treated with Tob–SS–Tob NPs and Tob–SS–Gm NPs exhibited a pronounced reduction in bacterial burden compared with the control group. In contrast, Gm–SS–Gm NPs showed a negligible effect on intratumoral bacterial burden, highlighting the superiority of the AiDCs strategy in bacterial eradication. Motivated by the efficient bacterial elimination and tumor cell killing, we speculate that the slices of bacteria and tumor cells could activate the immune response via pathogen-associated molecular patterns (PAMPs) and damage-associated molecular patterns (DAMPs)[48,49]. Consistent with this hypothesis, immunohistochemical staining revealed significantly elevated expression of calreticulin (CRT) and high-mobility group box 1 (HMGB1) in tumors treated with Tob–SS–Gm NPs (Fig. 7B, C, E&F), both of which are well-established hallmarks of immunogenic cell death (ICD) [50]. Notably, the expression levels of CRT and HMGB1 in the Tob–SS–Gm NPs group were markedly higher than those in the Gm–SS–Gm NPs group, suggesting that bacterial elimination further amplifies ICD-associated danger signaling [51]. In addition, cleaved Caspase1, a key mediator of inflammasome activation [52,53], was significantly upregulated in the Tob–SS–Gm NPs group (Fig. 7D and G), indicating the activation of pro-inflammatory signaling pathways that may facilitate immune cell recruitment and activation.

To further characterize the downstream immune response, the dendritic cell (DC)-T cell axis was evaluated. Flow cytometry analysis demonstrated that the proportion of mature DCs ($CD80^+CD86^+$) in tumor-draining lymph nodes was significantly increased following Tob–SS–Gm NPs treatment, reaching 84.9%, which was nearly twofold higher than that observed in the Gm–SS–Gm NPs group (Fig. 7H and I, Fig. S30, Supporting Information). Mechanistically, DAMPs such as CRT and HMGB1, together with PAMPs derived from bacterial components, are known to be recognized by pattern recognition receptors such as TLR2/4/9, thereby promoting DCs maturation and antigen-presenting capacity [54,55]. Consistent with enhanced DCs activation, a robust cytotoxic T cell response was observed. Immunofluorescence staining

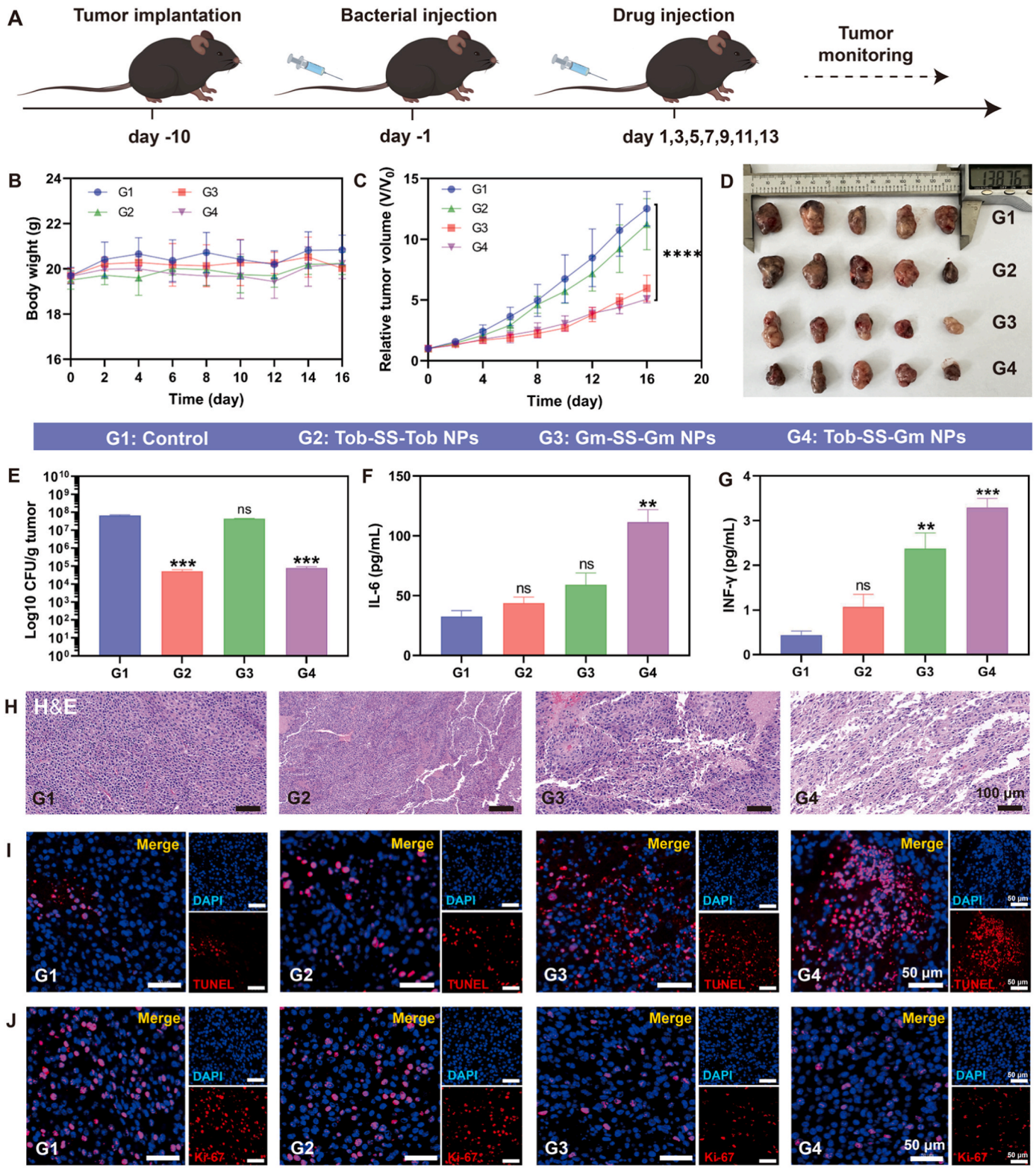
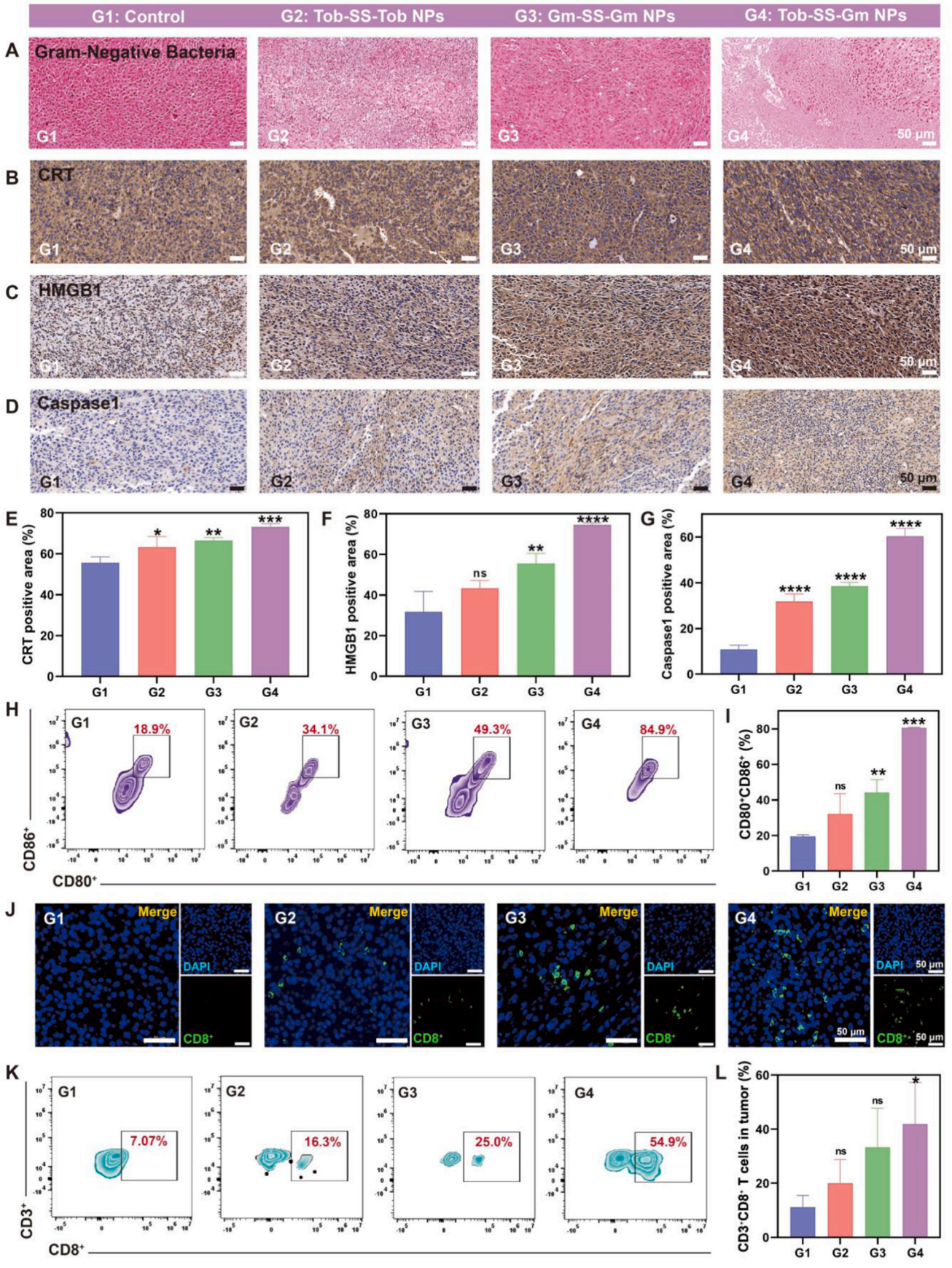


Fig. 6. *In vivo* antitumor efficacy of AiDCs in an intratumoral *E. coli*–colonized Panc02 tumor model. (A) Schematic illustration of the establishment of the mouse tumor model and the *in vivo* treatment protocol. (B) Average body weight of mice in each group during the therapeutic period. (C) Relative tumor volume changes over a 16 day treatment period. (D) Representative photographs of excised tumor tissues from each group after 16 days of treatment. (E) CFU of residual *E. coli* in tumors after different treatments for 16 days. (F&G) Enzyme-linked immunosorbent assay (ELISA) analysis of serum interleukin-6 (IL-6) and interferon-γ (IFN-γ) levels after different treatments for 16 days. (H-J) Hematoxylin and eosin (H&E), TUNEL, and Ki-67 staining of tumor tissue sections from each treatment group.



(caption on next page)

Fig. 7. *In vivo* activation of antitumor immune responses induced by Tob–SS–Gm NPs. (A) Gram staining images of tumor tissues after different treatments. (B) Immunohistochemical staining images of calreticulin (CRT) in tumor tissues after different treatments. (C) Immunohistochemical staining images of high-mobility group box 1 (HMGB1) in tumor tissues after various treatments. (D) Immunohistochemical staining images of Caspase1 in tumor tissues after various treatments. (E-G) Quantitative analysis of CRT, HMGB1, and Caspase1 fluorescence signals based on ImageJ analysis. (H&I) Representative flow cytometry (FCM) plots and quantitative analysis of mature DCs ($CD80^+CD86^+$) in tumor-draining lymph nodes after different treatments. (J) Immunofluorescence images of $CD8^+$ T-cell infiltration in tumor tissues after different treatments. (K&L) Representative FCM plots and quantitative analysis of $CD8^+$ T cells in tumor tissues after different treatments.

revealed markedly increased infiltration of $CD8^+$ T cells in tumor tissues following Tob–SS–Gm NPs treatment (Fig. 7J). Quantitative flow cytometry further confirmed a substantial increase in $CD8^+$ T cell populations, from 7.1% in the control group to 54.9% in the treated group (Fig. 7K and L, Fig. S31, Supporting Information). Similar trends were observed in systemic immune organs, including the spleen and lymph nodes. Specifically, the proportion of $CD8^+$ T cells increased from 14.7% to 49.9% in spleen tissues (Fig. S32, Supporting Information) and from 9.48% to 75% in lymph nodes (Fig. S33, Supporting Information), suggesting the activation of systemic immune responses associated with antitumor activity. Taken together, these results suggest that Tob–SS–Gm NPs are associated with immune remodeling through coordinated bacterial elimination and tumor cell killing, leading to enhanced DAMP/PAMP signaling, DCs maturation, and subsequent $CD8^+$ T cell-mediated antitumor immunity.

In addition to adaptive immune activation, the tumor immune microenvironment was further characterized at the cellular level. As shown in Figs. S34 and 35, Supporting Information, Tob–SS–Gm NPs treatment significantly reduced the infiltration of immunosuppressive cells, including $LY6G^+$ myeloid-derived suppressor cells (MDSCs) and $FOXP3^+$ regulatory T cells (Tregs). Meanwhile, macrophage polarization analysis revealed a shift toward a pro-inflammatory phenotype, as evidenced by increased $CD86^+$ (M1-like) and decreased $CD206^+$ (M2-like) macrophages (Fig. S36, Supporting Information). Furthermore, enhanced cytotoxic immune activity within the tumor microenvironment was supported by increased numbers of Granzyme B^+ and IFN-γ^+ cells (Fig. S37 and 38, Supporting Information). These findings collectively indicate that Tob–SS–Gm NPs not only activate adaptive immune responses but also effectively alleviate immunosuppression and promote a cytotoxic immune milieu. Taken together, these results demonstrate that Tob–SS–Gm NPs induce a comprehensive remodeling of the tumor immune microenvironment through coordinated bacterial elimination and tumor cell killing. This process enhances DAMP/PAMP signaling, promotes DCs maturation, and subsequently drives $CD8^+$ T cell-mediated antitumor immunity, ultimately contributing to the observed synergistic chemo-immunotherapeutic effect [56]. These findings are consistent with previous reports demonstrating that immunogenic regulated cell death can effectively stimulate antitumor immune responses [57–59].

3.8. Molecular mechanisms assisted by eradicating intratumoral bacteria

To elucidate the molecular mechanisms by which Tob–SS–Gm nanoparticles (NPs) eradicate intratumoral bacteria and thereby sensitize pancreatic cancer to gemcitabine chemotherapy, we performed comparative transcriptomic profiling of Panc02 cells treated with Tob–SS–Gm NPs, with or without bacterial colonization. Three groups were analyzed: Group i, untreated Panc02 + *E. coli* cells; Group ii, Panc02 + *E. coli* cells treated with Tob–SS–Gm NPs; and Group iii, Panc02 cells treated with Tob–SS–Gm NPs. Global gene-expression distributions (Fig. 8A) revealed highly consistent FPKM boxplots across all samples, indicating uniform sequencing quality and comparable gene coverage. Sample-sample correlation heatmaps (Fig. 8B) showed intra-group correlation coefficients exceeding 0.9, confirming data robustness and reproducibility. Notably, gene-expression patterns in Group ii were clearly segregated from Group i, suggesting substantial transcriptomic remodeling associated with bacterial clearance (Fig. 8C). In contrast, Group ii and Group iii exhibited only modest divergence, suggesting that the dominant biological effect of Tob–SS–Gm NPs arises not from the chemotherapeutic component (Gm) alone but from Tob-mediated bacterial elimination and consequent microenvironmental and signaling rewiring. A Venn diagram (Fig. 8D) indicated that 10,219 genes were commonly expressed across groups, while each pairwise comparison displayed substantial numbers of group-specific differentially expressed genes (DEGs). DEGs analysis showed that the ii vs i comparison directly reflects the molecular consequences of bacterial clearance underlying enhanced gemcitabine sensitivity (Fig. 8E). A total of 215 genes were upregulated, whereas 2806 were significantly downregulated, indicating extensive transcriptomic reprogramming following bacterial removal. By comparison, the number of DEGs in ii vs iii was substantially smaller (376 upregulated and 237 downregulated (Fig. 8F), supporting the conclusion that the therapeutic efficacy of Tob–SS–Gm NPs is primarily driven by intratumoral bacterial eradication rather than by gemcitabine alone. These findings reinforce the concept that intratumoral bacteria play a critical role in pancreatic cancer chemoresistance.

GO enrichment analysis further illuminated the molecular basis of the antibacterial effect on tumor-cell behavior. In ii vs i (Fig. 8G and H), gene sets associated with microtubule-based movement, microtubule-based processes, cytoskeleton organization, and cytoskeletal protein binding were upregulated, indicating that bacterial depletion enhances gemcitabine sensitivity by modulating cytoskeletal dynamics and intercellular communication. Conversely, pathways related to the regulation of transcription, regulation of RNA metabolism, DNA repair, RNA biosynthetic processes, and catalytic activities acting on DNA were downregulated, which may be associated with altered cellular stress responses and proliferation states. In ii vs iii (Fig. 8I and J), pathways associated with DNA repair and RNA biosynthesis also showed reduced activity, further indicating that bacterial presence is linked to distinct transcriptional regulation during treatment. KEGG pathway analysis revealed that in ii vs i (Figs. S39 and 40, Supporting Information), pathways associated with cell death processes, such as ferroptosis and necroptosis, were upregulated, suggesting that bacterial clearance sensitizes tumors to chemotherapy-induced oxidative stress and apoptosis. Meanwhile, bacterial resistance-related pathways-including NOD-like receptor signaling, PI3K-Akt signaling, and peroxisome pathways-were downregulated, indicating suppression of resistance mechanisms. In ii vs iii (Fig. S41 and 42, Supporting Information), pathways such as PPAR signaling, lipid and atherosclerosis signaling, spliceosome activity, and the one-carbon pool by folate were upregulated, demonstrating increased activity in lipid metabolism, nucleotide synthesis, and RNA-processing pathways following bacterial removal. At the same time, the ErbB signaling pathway, EGFR tyrosine-kinase inhibitor resistance and inflammatory mediator regulation of TRP channels were downregulated, reflecting reduced stemness and survival signaling and thus increased chemosensitivity. Collectively, these data indicate that bacterial clearance in Group ii is associated with a distinct transcriptional state characterized by alterations in metabolic activity, stress responses, and survival-related pathways, which may contribute to the enhanced therapeutic response to Gm. Notably, these transcriptomic findings should be interpreted as indicative of potential biological processes rather than direct evidence of causality.

4. Conclusions

In summary, this study presents an innovative AiDCs strategy

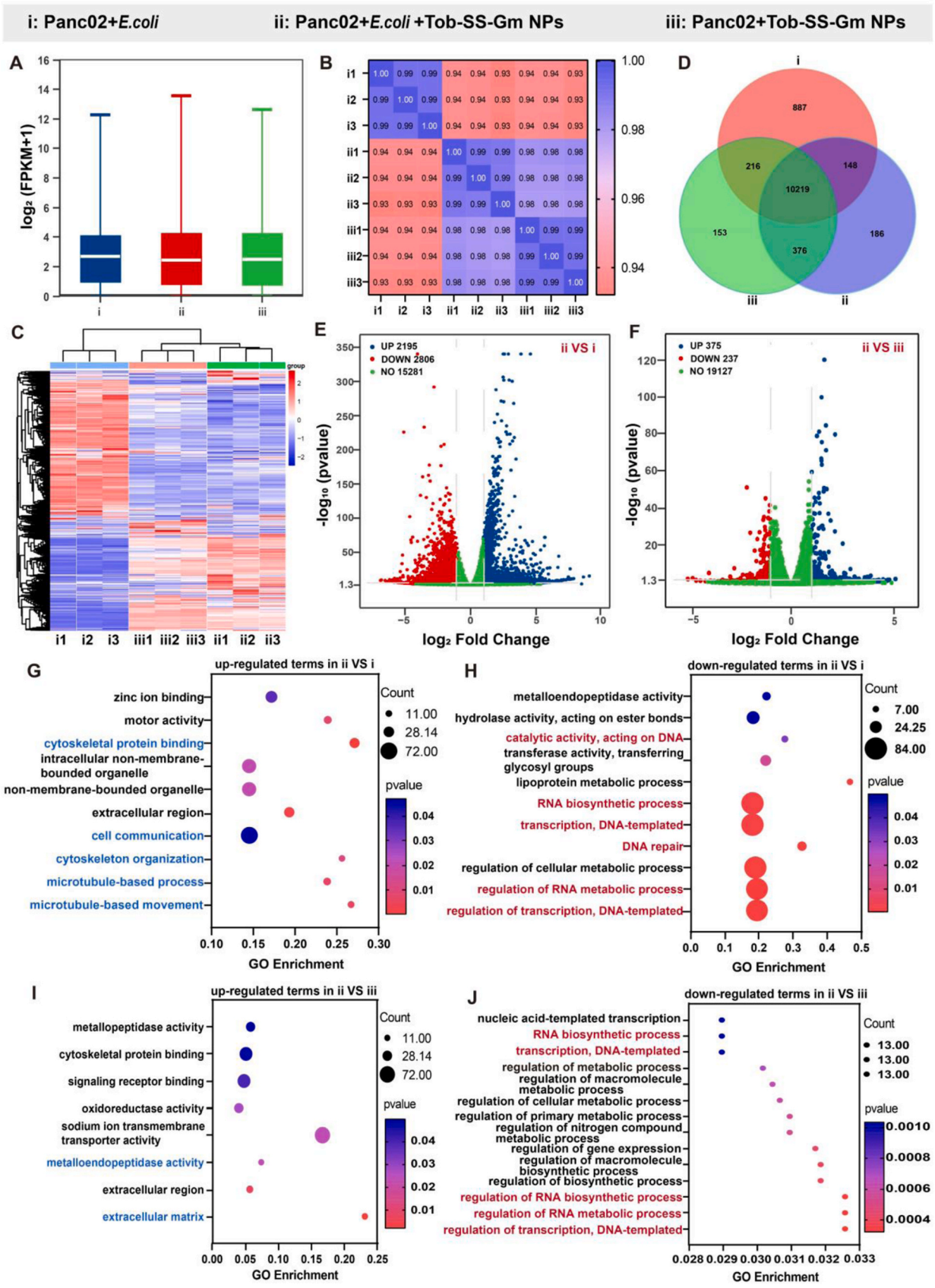


Fig. 8. Transcriptomic analysis revealing molecular mechanisms. (A) Transcript abundance (log_2(FPKM+1)) in groups i, ii, and iii. (B) Pearson correlation analysis of all RNA-seq samples. (C) Hierarchical clustering heatmap of differentially expressed genes (DEGs). (D) Venn diagram showing the overlap of DEGs among different groups. (E&F) Volcano plots of DEGs in ii vs i and ii vs iii, respectively. (G&H) Gene Ontology (GO) enrichment analysis of up- and down-regulated terms in ii vs i. (I&J) GO enrichment analysis of up- and down-regulated terms in ii vs iii.

(Tob–SS–Gm NPs) to enhance chemotherapy efficacy of Gm for pancreatic cancer by eliminating intratumoral bacteria. The integration of Tob and Gm perfectly meets the requirements for intratumoral bacterial clearance during chemotherapy. Tob–SS–Gm NPs are conjugated via dynamic disulfide bonds, which enables these AiDCs to remain stable under physiological conditions but undergo rapid cleavage in the high GSH tumor microenvironment, releasing antibacterial activity against *E. coli* and chemotherapeutic activity for Panc02 cells. Both *in vitro* and *in vivo* evaluations demonstrated that Tob–SS–Gm NPs significantly reduced intratumoral bacterial burden and improved the therapeutic response to gemcitabine under bacteria-colonized tumor conditions. Furthermore, bacterial eradication and tumor-cell damage were accompanied by remodeling of the tumor immune microenvironment, including enhanced dendritic-cell maturation and cytotoxic $CD8^+$ T-cell activation. Collectively, these findings highlight the potential of the AiDC strategy as a promising therapeutic approach for intratumoral bacteria-associated, drug-resistant malignancies.

CRediT authorship contribution statement

Ziyao Zhang: Conceptualization, Investigation, Methodology, Software, Visualization, Writing – original draft, Writing – review & editing. **Fangming Zhang:** Investigation, Methodology, Software, Visualization, Writing – review & editing. **Wangting Yang:** Methodology, Software, Visualization, Writing – review & editing. **Jingxia Xu:** Investigation, Methodology, Software, Writing – review & editing. **Zhuyuan Peng:** Methodology, Software, Writing – review & editing. **Xinyu Zhao:** Methodology, Software, Writing – review & editing. **Yen Wei:** Methodology, Writing – review & editing. **Guofeng Li:** Conceptualization, Methodology, Visualization, Writing – review & editing. **Wensheng Xie:** Conceptualization, Funding acquisition, Investigation, Methodology, Visualization, Writing – original draft, Writing – review & editing. **Xing Wang:** Conceptualization, Funding acquisition, Writing – review & editing.

Declaration of competing interest

The authors declare that they have no known competing financial interests or personal relationships that could have appeared to influence the work reported in this paper.

Acknowledgements

This work was supported by the Natural Science Foundation of Beijing Municipality (2254093) and the National Natural Science Foundation of China (52273118, 22275013). Many thanks to the Interdisciplinary Research Center of Beijing University of Chemical Technology (XK2025-05) and the Fundamental Research Funds for the Central Universities (buctrc202419).

Appendix A. Supplementary data

Supplementary data to this article can be found online at https://doi.org/10.1016/j.biomaterials.2026.124368.

Data availability

Data will be made available on request.

References

[1] T.F. Stoop, A.A. Javed, A. Oba, B.G. Koerkamp, T. Seufferlein, J.W. Wilmink, M. G. Besselink, Pancreatic cancer, Lancet 405 (2025) 1182–1202, https://doi.org/10.1016/S0140-6736(25)00261-2.

[2] J.D. Mizrahi, R. Surana, J.W. Valle, R.T. Shroff, Pancreatic cancer, Lancet 395 (2020) 2008–2020, https://doi.org/10.1016/S0140-6736(20)30974-0.

[3] Q. Zhou, S. Shao, J. Wang, C. Xu, J. Xiang, Y. Piao, Z. Zhou, Q. Yu, J. Tang, X. Liu, Z. Gan, R. Mo, Z. Gu, Y. Shen, Enzyme-activatable polymer–drug conjugate augments tumour penetration and treatment efficacy, Nat. Nanotechnol. 14 (2019) 799–809, https://doi.org/10.1038/s41565-019-0485-z.

[4] A. Mannucci, A. Goel, Advances in pancreatic cancer early diagnosis, prevention, and treatment: the past, the present, and the future, CA Cancer J. Clin. (2025), https://doi.org/10.3322/caac.70035 caac.70035.

[5] T. Kamisawa, L.D. Wood, T. Itoi, K. Takaori, Pancreatic cancer, Lancet 388 (2016) 73–85, https://doi.org/10.1016/S0140-6736(16)00141-0.

[6] J. Zhang, S. Lv, X. Peng, H. Liu, J. Guo, Z. Liu, T. Chu, H. Liu, K. Duan, F. Lou, Y. Chi, B. Gao, Y. Liu, F. Wei, CircERC1 facilitates chemoresistance through inhibiting pyroptosis and remodeling extracellular matrix in pancreatic cancer, Mol. Cancer 24 (2025) 185, https://doi.org/10.1186/s12943-025-02385-9.

[7] Y. Zhu, Y. Huang, Y. Shi, C. Huang, G. Zhao, Z. Liu, M. Ma, J. Ye, X. Xu, Q. Liu, X. Huang, J. Wang, Q. Xu, X. Yin, Epigenetic activation of the CMTM6-IGF2BP1-EP300 positive feedback loop drives gemcitabine resistance in pancreatic ductal adenocarcinoma, Adv. Sci. 11 (2024) 2406714, https://doi.org/10.1002/advs.202406714.

[8] V. Chandra, F. McAllister, Therapeutic potential of microbial modulation in pancreatic cancer, Gut 70 (2021) 1419–1425, https://doi.org/10.1136/gutjnl-2019-319807.

[9] D. Nejman, I. Livyatan, G. Fuks, N. Gavert, Y. Zwang, L.T. Geller, A. Rotter-Maskowitz, R. Weiser, G. Mallel, E. Gigi, A. Meltser, G.M. Douglas, I. Kamer, V. Gopalakrishnan, T. Dadosh, S. Levin-Zaidman, S. Avnet, T. Atlan, Z.A. Cooper, R. Arora, A.P. Cogdill, M.A.W. Khan, G. Ologun, Y. Bussi, A. Weinberger, M. Lotan-Pompan, O. Golani, G. Perry, M. Rokah, K. Bahar-Shany, E.A. Rozeman, C.U. Blank, A. Ronai, R. Shaoul, A. Amit, T. Dorfman, R. Kremer, Z.R. Cohen, S. Harnof, T. Siegal, E. Yehuda-Shnaidman, E.N. Gal-Yam, H. Shapira, N. Baldini, M.G. I. Langille, A. Ben-Nun, B. Kaufman, A. Nissan, T. Golan, M. Dadiani, K. Levanon, J. Bar, S. Yust-Katz, I. Barshack, D.S. Peeper, D.J. Raz, E. Segal, J.A. Wargo, J. Sandbank, N. Shental, R. Straussman, The human tumor microbiome is composed of tumor type-specific intracellular bacteria, Science 368 (2020) 973–980, https://doi.org/10.1126/science.aay9189.

[10] A. Fu, B. Yao, T. Dong, Y. Chen, J. Yao, Y. Liu, H. Li, H. Bai, X. Liu, Y. Zhang, C. Wang, Y. Guo, N. Li, S. Cai, Tumor-resident intracellular microbiota promotes metastatic colonization in breast cancer, Cell 185 (2022) 1356–1372.e26, https://doi.org/10.1016/j.cell.2022.02.027.

[11] M. Carstensen, L.-M. Philipp, M. Basu, P. Hoffmann, J.-N. Klenig, A. M. Wandmacher, S. Sebens, Intratumoral microbiome and pancreatic cancer: an enabling hallmark and path to novel treatments? Br. J. Cancer (2025) https://doi.org/10.1038/s41416-025-03324-7.

[12] L.T. Geller, M. Barzily-Rokni, T. Danino, O.H. Jonas, N. Shental, D. Nejman, N. Gavert, Y. Zwang, Z.A. Cooper, K. Shee, C.A. Thaiss, A. Reuben, J. Livny, R. Avraham, D.T. Frederick, M. Ligorio, K. Chatman, S.E. Johnston, C.M. Mosher, A. Brandis, G. Fuks, C. Gurbatri, V. Gopalakrishnan, M. Kim, M.W. Hurd, M. Katz, J. Fleming, A. Maitra, D.A. Smith, M. Skalak, J. Bu, M. Michaud, S.A. Trauger, I. Barshack, T. Golan, J. Sandbank, K.T. Flaherty, A. Mandinova, W.S. Garrett, S. P. Thayer, C.R. Ferrone, C. Huttenhower, S.N. Bhatia, D. Gevers, J.A. Wargo, T. R. Golub, R. Straussman, Potential role of intratumor bacteria in mediating tumor resistance to the chemotherapeutic drug gemcitabine, Science 357 (2017) 1156–1160, https://doi.org/10.1126/science.aah5043.

[13] X. Kang, F. Bu, W. Feng, F. Liu, X. Yang, H. Li, Y. Yu, G. Li, H. Xiao, X. Wang, Dual-cascade responsive nanoparticles enhance pancreatic cancer therapy by eliminating tumor-resident intracellular bacteria, Adv. Mater. 34 (2022) 2206765, https://doi.org/10.1002/adma.202206765.

[14] Y. Xie, J. Wang, L. Li, M. Wang, J. Sun, J. Chang, J. Lin, C. Li, A metal chelation therapy to effectively eliminate breast cancer and intratumor bacteria while suppressing tumor metastasis by copper depletion and zinc ions surge, Angew. Chem. Int. Ed. 64 (2025) e202417592, https://doi.org/10.1002/anie.202417592.

[15] S. Geng, P. Guo, X. Li, Y. Shi, J. Wang, M. Cao, Y. Zhang, K. Zhang, A. Li, H. Song, Z. Zhang, J. Shi, J. Liu, Y. Yang, Biomimetic nanovehicle-enabled targeted depletion of intratumoral fusobacterium nucleatum synergizes with PD-l1 blockade against breast cancer, ACS Nano 18 (2024) 8971–8987, https://doi.org/10.1021/acsnano.3c12687.

[16] Q. Chen, Y. Zhu, K. Wang, X. Wang, Y. Zhang, M. Zhou, J. Du, X. Qu, Z. Shi, Y. Zhang, Y. Chen, H. Qin, Clearing intratumoral bacteria to augment tumor-therapeutic response by engineering antimicrobial dendritic mesoporous silica nanomedicine, Nano Today 52 (2023) 101994, https://doi.org/10.1016/j.nantod.2023.101994.

[17] M. Wang, B. Rousseau, K. Qiu, G. Huang, Y. Zhang, H. Su, C. Le Bihan-Benjamin, I. Khati, O. Artz, M.B. Foote, Y.-Y. Cheng, K.-H. Lee, M.Z. Miao, Y. Sun, P.-J. Bousquet, M. Hilmi, E. Dumas, A.-S. Hamy, F. Reyal, L. Lin, P.M. Armistead, W. Song, A. Vargason, J.C. Arthur, Y. Liu, J. Guo, X. Zhou, J. Nguyen, Y. He, J.P.-Y. Ting, A.C. Anselmo, L. Huang, Killing tumor-associated bacteria with a liposomal antibiotic generates neoantigens that induce anti-tumor immune responses, Nat. Biotechnol. 42 (2024) 1263–1274, https://doi.org/10.1038/s41587-023-01957-8.

[18] Y. Wang, Y. Han, C. Yang, T. Bai, C. Zhang, Z. Wang, Y. Sun, Y. Hu, F. Besenbacher, C. Chen, M. Yu, Long-term relapse-free survival enabled by integrating targeted antibacteria in antitumor treatment, Nat. Commun. 15 (2024) 4194, https://doi.org/10.1038/s41467-024-48662-x.

[19] L. Maier, C.V. Goemans, J. Wirbel, M. Kuhn, C. Eberl, M. Pruteanu, P. Müller, S. Garcia-Santamarina, E. Cacace, B. Zhang, C. Gekeler, T. Banerjee, E.E. Anderson, A. Milanese, U. Löber, S.K. Forslund, K.R. Patil, M. Zimmermann, B. Stecher, G. Zeller, P. Bork, A. Typas, Unravelling the collateral damage of antibiotics on gut

bacteria, Nature 599 (2021) 120–124, https://doi.org/10.1038/s41586-021-03986-2.
[20] A.C. Fenneman, M. Weidner, L.A. Chen, M. Nieuwdorp, M.J. Blaser, Antibiotics in the pathogenesis of diabetes and inflammatory diseases of the gastrointestinal tract, Nat. Rev. Gastroenterol. Hepatol. 20 (2023) 81–100, https://doi.org/10.1038/s41575-022-00685-9.
[21] H. Szajewska, K.P. Scott, T. De Meij, S.K. Forslund-Startceva, R. Knight, O. Koren, P. Little, B.C. Johnston, J. Łukasik, J. Suez, D.J. Tancredi, M.E. Sanders, Antibiotic-perturbed microbiota and the role of probiotics, Nat. Rev. Gastroenterol. Hepatol. 22 (2025) 155–172, https://doi.org/10.1038/s41575-024-01023-x.
[22] A. Nikoletic, E. Natsaridis, T. Flathmann, D.P.C. Quadros, N. Gogniat, O. Tagit, Soft nanocarriers as antimicrobial co-delivery systems to combat resistant infections, Adv. Healthcare Mater. 14 (2025) 2404540, https://doi.org/10.1002/adhm.202404540.
[23] Z. Sabeel, Z. Yang, Microbiome-targeted nanoplatforms and engineering approaches in breast cancer therapy, Mol. Cancer 24 (2025) 276, https://doi.org/10.1186/s12943-025-02456-x.
[24] T. Lang, R. Zhu, X. Zhu, W. Yan, Y. Li, Y. Zhai, T. Wu, X. Huang, Q. Yin, Y. Li, Combining gut microbiota modulation and chemotherapy by capecitabine-loaded prebiotic nanoparticle improves colorectal cancer therapy, Nat. Commun. 14 (2023) 4746, https://doi.org/10.1038/s41467-023-40439-y.
[25] X. Zhang, N. Li, S. Zhang, B. Sun, Q. Chen, Z. He, C. Luo, J. Sun, Emerging carrier-free nanosystems based on molecular self-assembly of pure drugs for cancer therapy, Med. Res. Rev. 40 (2020) 1754–1775, https://doi.org/10.1002/med.21669.
[26] D. Wang, F. Yin, Z. Li, Y. Zhang, C. Shi, Current progress and remaining challenges of peptide–drug conjugates (PDCs): next generation of antibody-drug conjugates (ADCs)? J. Nanobiotechnol. 23 (2025) 305, https://doi.org/10.1186/s12951-025-03277-2.
[27] L. Li, T. Liu, S. Zuo, Y. Li, E. Zhao, Q. Lu, D. Wang, Y. Sun, Z. He, B. Sun, J. Sun, Satellite-type sulfur atom distribution in trithiocarbonate bond-bridged dimeric prodrug nanoassemblies: achieving both stability and activatability, Adv. Mater. 36 (2024) 2310633, https://doi.org/10.1002/adma.202310633.
[28] X. Kong, X. Xie, J. Wu, X. Wang, W. Zhang, S. Wang, D.V. Abbasova, Y. Fang, H. Jiang, J. Gao, J. Wang, Combating cancer immunotherapy resistance: a nano-medicine perspective, Cancer Commun. 45 (2025) 813–840, https://doi.org/10.1002/cac2.70025.
[29] J. Zheng, H. Ge, D. Zhou, Q. Yao, S. Long, W. Sun, J. Fan, J. Du, X. Peng, An activatable prodrug nanosystem for ultrasound-driven multimodal tumor therapy and metastasis inhibition, Adv. Mater. 35 (2023) 2308205, https://doi.org/10.1002/adma.202308205.
[30] Y. Fu, J. Yang, L. Huang, F. Liu, F. Bu, X. Kang, G. Li, Q. Ren, T.F. Moriarty, X. Wang, Self-carrier nanodrugs with dual antibacterial agents to overcome tobramycin resistance in multidrug-resistant staphylococcus aureus, Bioact. Mater. 56 (2026) 386–401, https://doi.org/10.1016/j.bioactmat.2025.10.022.
[31] Y. Yang, B. Sun, S. Zuo, X. Li, S. Zhou, L. Li, C. Luo, H. Liu, M. Cheng, Y. Wang, S. Wang, Z. He, J. Sun, Trisulfide bond–mediated doxorubicin dimeric prodrug nanoassemblies with high drug loading, high self-assembly stability, and high tumor selectivity, Sci. Adv. 6 (2020), https://doi.org/10.1126/sciadv.abc1725 eabc1725.
[32] D. Zhao, W. Tao, S. Li, Y. Chen, Y. Sun, Z. He, B. Sun, J. Sun, Apoptotic body–mediated intercellular delivery for enhanced drug penetration and whole tumor destruction, Sci. Adv. 7 (2021), https://doi.org/10.1126/sciadv.abg0880 eabg0880.
[33] Z. Yao, Q. Hu, P. Jin, B. Li, Y. Huang, F. Zhang, M. Wang, J. Huang, J. Huang, S. Shao, X. Zhao, Y. Ping, T. Liang, A self-assembly combined nano-prodrug to overcome gemcitabine chemo-resistance of pancreatic tumors, Adv. Funct. Mater. 33 (2023) 2214598, https://doi.org/10.1002/adfm.202214598.
[34] B.H. Pogostin, S.X. Wu, M.J. Swierczynski, C. Pennington, S.-Y. Li, D. Vohidova, E. H. Seeley, A. Agrawal, C. Tang, M.H. Yu, A. Dey, S. Hernandez, J. Cabler, O. Veiseh, E.L. Nuermberger, Z.T. Ball, J.D. Hartgerink, K.J. McHugh, Nanofibrous supramolecular peptide hydrogels for controlled release of small-molecule drugs and biologics, Nat. Nanotechnol. 20 (2025) 1502–1513, https://doi.org/10.1038/s41565-025-01981-6.
[35] M. Hou, P. Xue, Y.-E. Gao, X. Ma, S. Bai, Y. Kang, Z. Xu, Gemcitabine–camptothecin conjugates: a hybrid prodrug for controlled drug release and synergistic therapeutics, Biomater. Sci. 5 (2017) 1889–1897, https://doi.org/10.1039/C7BM00382J.
[36] H. Shi, Y. Luo, S. Zhang, M. Zhao, C. Liu, Q. Pei, H. Wang, Q. Dai, Z. Xie, B. Xu, W. Tian, Dual-responsive nanogels with high drug loading for enhanced tumor targeting and treatment, Chin. Chem. Lett. 36 (2025) 110775, https://doi.org/10.1016/j.cclet.2024.110775.
[37] Y. Li, Q. Pei, B. Cui, H. Zhang, L. Han, W. Li, W. Zhu, X. Feng, Z. Xie, A redox-responsive dihydroartemisinin dimeric nanoprodrug for enhanced antitumor activity, J. Nanobiotechnol. 19 (2021) 441, https://doi.org/10.1186/s12951-021-01200-z.
[38] C. Gao, X. Wang, B. Yang, W. Yuan, W. Huang, G. Wu, J. Ma, Synergistic target of intratumoral microbiome and tumor by metronidazole–fluorouridine nanoparticles, ACS Nano 17 (2023) 7335–7351, https://doi.org/10.1021/acsnano.2c11305.
[39] G. Ramage, R. Kean, R. Rautemaa-Richardson, C. Williams, J.L. Lopez-Ribot, Fungal biofilms in human health and disease, Nat. Rev. Microbiol. 23 (2025) 355–370, https://doi.org/10.1038/s41579-025-01147-0.
[40] C. Chen, S. Wang, W. Niu, F. Liu, W. Xie, G. Li, D. Kong, X. Wang, Synergistic effects of borneol and zwitterionic coating on enhanced antimicrobial and anti-biofilm performance, Colloids Surf. B Biointerfaces 255 (2025) 114929, https://doi.org/10.1016/j.colsurfb.2025.114929.
[41] S. Arya Jyoti, X. Peng, M. Pumera, Virus enhanced microrobots for biofilm eradication, Adv. Mater. 37 (2025) e08299, https://doi.org/10.1002/adma.202508299.
[42] G. Yu, J. Ding, N. Yang, L. Ge, N. Chen, X. Zhang, Q. Wang, X. Liu, X. Zhang, X. Jiang, Y. Geng, C. Zhang, J. Pan, X. Wang, W. Gao, Z. Li, H. Zhang, W. Ni, J. Xiao, K. Zhou, L. Yang, Evaluating the pro-survival potential of apoptotic bodies derived from 2D- and 3D- cultured adipose stem cells in ischaemic flaps, J. Nanobiotechnol. 22 (2024) 333, https://doi.org/10.1186/s12951-024-02533-1.
[43] Z. Wu, X. Lin, Y. Ying, G. Fan, J. Shi, X. Zheng, B. Hu, H. Che, H. Chen, W. Yang, X. Fan, K. Mo, J. Wu, Z. Lan, Z. Yu, S. Wang, C. Cui, A dual-targeting strategy to inhibit colorectal cancer liver metastasis via tumor cell ferroptosis and cancer-associated fibroblast reprogramming, Bioact. Mater. 52 (2025) 73–91, https://doi.org/10.1016/j.bioactmat.2025.05.025.
[44] B. Xu, Y. Cui, W. Wang, S. Li, C. Lyu, S. Wang, W. Bao, H. Wang, M. Qin, Z. Liu, W. Wei, H. Liu, Immunomodulation-enhanced nanozyme-based tumor catalytic therapy, Adv. Mater. 32 (2020) 2003563, https://doi.org/10.1002/adma.202003563.
[45] R. Van Der Meel, E. Sulheim, Y. Shi, F. Kiessling, W.J.M. Mulder, T. Lammers, Smart cancer nanomedicine, Nat. Nanotechnol. 14 (2019) 1007–1017, https://doi.org/10.1038/s41565-019-0567-y.
[46] M.J. Mitchell, M.M. Billingsley, R.M. Haley, M.E. Wechsler, N.A. Peppas, R. Langer, Engineering precision nanoparticles for drug delivery, Nat. Rev. Drug Discov. 20 (2021) 101–124, https://doi.org/10.1038/s41573-020-0090-8.
[47] Q. Chen, L. Yuan, W.-C. Chou, Y.-H. Cheng, C. He, N.A. Monteiro-Riviere, J. E. Riviere, Z. Lin, Meta-analysis of nanoparticle distribution in tumors and major organs in tumor-bearing mice, ACS Nano 17 (2023) 19810–19831, https://doi.org/10.1021/acsnano.3c04037.
[48] H. Guo, J.B. Callaway, J.P.-Y. Ting, Inflammasomes: mechanism of action, role in disease, and therapeutics, Nat. Med. 21 (2015) 677–687, https://doi.org/10.1038/nm.3893.
[49] M. Ma, W. Jiang, R. Zhou, DAMPs and DAMP-sensing receptors in inflammation and diseases, Immunity 57 (2024) 752–771, https://doi.org/10.1016/j.immuni.2024.03.002.
[50] F. Zhang, Z. Zhang, W. Yang, Z. Peng, J. Sun, G. Li, Y. Wei, X. Wang, L. Zhao, W. Xie, Engineering autologous cell-derived exosomes to boost melanoma-targeted radio-immunotherapy by cascade cGAS-STING pathway activation, Small 21 (2025) 2408769, https://doi.org/10.1002/smll.202408769.
[51] Y. Xie, J. Wang, Y. Han, G. Zhu, L. Li, Q. Sun, C. Li, Antagonistic iron competition induced by iron chelators heightens cuproptosis in both tumors and intratumoral bacteria, Adv. Mater. 38 (2026) e15904, https://doi.org/10.1002/adma.202515904.
[52] C. Ross, A.H. Chan, J.B. Von Pein, M.P. Maddugoda, D. Boucher, K. Schroder, Inflammatory caspases: toward a unified model for caspase activation by inflammasomes, Annu. Rev. Immunol. 40 (2022) 249–269, https://doi.org/10.1146/annurev-immunol-101220-030653.
[53] W. Zheng, W. Marini, K. Murakami, V. Sotov, M. Butler, C. Gorrini, P.S. Ohashi, M. Reedijk, Caspase-1-dependent spatiality in triple-negative breast cancer and response to immunotherapy, Nat. Commun. 15 (2024) 8514, https://doi.org/10.1038/s41467-024-52553-6.
[54] B. Li, G. Hao, B. Sun, Z. Gu, Z.P. Xu, Engineering a therapy-induced “immunogenic cancer cell death” amplifier to boost systemic tumor elimination, Adv. Funct. Mater. 30 (2020) 1909745, https://doi.org/10.1002/adfm.201909745.
[55] S. Rakoff-Nahoum, J. Paglino, F. Eslami-Varzaneh, S. Edberg, R. Medzhitov, Recognition of commensal microflora by toll-like receptors is required for intestinal homeostasis, Cell 118 (2004) 229–241, https://doi.org/10.1016/j.cell.2004.07.002.
[56] S. Wang, S. Li, M. Zhang, R. Liu, X. Ye, S. Mao, J. Yu, X. Xie, W. Tan, Unraveling the role of the microbiota in cancer immunotherapy: a new frontier, Research 8 (2025) 744, https://doi.org/10.34133/research.0744.
[57] G. Jiang, F. Zhang, Z. Wu, X. Zhang, J. Xu, Z. Peng, G. Li, G. Zhu, X. Wang, W. Xie, Targeting mitochondrial oxidative stress by calcium/copper/elesclomol tri-overloaded nanocages for osteosarcoma immunotherapy via immunogenic cell death, ACS Nano 19 (2025) 37600–37616, https://doi.org/10.1021/acsnano.5c08243.
[58] W. Xie, Y. Li, Z. Guo, J. Lu, G. Li, Z. Zhang, F. Zhang, Y. Wei, X. Wang, L. Zhao, FePd nanozyme- and SKN-encapsulated functional lipid nanoparticles for cancer nanotherapy via ROS-boosting necroptosis, ACS Appl. Mater. Interfaces 16 (2024) 18411–18421, https://doi.org/10.1021/acsami.3c18497.
[59] W. Yang, Z. Zhang, J. Xu, Z. Peng, F. Zhang, X. Zhao, G. Li, Y. Wei, L. Zhao, L. Wang, X. Wang, W. Xie, Enhancing necroptotic chemo-immunotherapy of breast cancer by reactive oxygen species generating lipid nanoparticles, ACS Appl. Nano Mater. 8 (2025) 14470–14480, https://doi.org/10.1021/acsanm.5c02985.